J. Fluid Mech. (2007), *vol.* 587, *pp.* 173–215.
doi:10.1017/S0022112007007306 Printed in the United Kingdom

Sound generated by instability wave/shock-cell interaction in supersonic jets

PRASUN K. RAY[1] AND SANJIVA K. LELE[1,2]

[1]Department of Mechanical Engineering, Stanford University, Stanford, CA 94305, USA

[2]Department of Aeronautics and Astronautics Stanford University, Stanford, CA 94305, USA

(Received 28 June 2006 and in revised form 30 April 2007)

Broadband shock-associated noise is an important component of the overall noise generated by modern airplanes. In this study, sound generated by the weakly nonlinear interaction between linear instability waves and the shock-cell structure in supersonic jets is investigated numerically in order to gain insight into the broadband shock-noise problem. The model formulation decomposes the overall flow into a mean flow, linear instability waves, the shock-cell structure and shock-noise. The mean flow is obtained by solving RANS equations with a $k-\epsilon$ model. Locally parallel stability equations are solved for the shock structure, and linear parabolized stability equations are solved for the instability waves. Then, source terms representing the instability wave/shock-cell interaction are assembled and the inhomogeneous linearized Euler equations are solved for the shock-noise. Three cases are considered, a cold under-expanded $M_j = 1.22$ jet, a hot under-expanded $M_j = 1.22$ jet, and a cold over-expanded $M_j = 1.36$ jet.

Shock-noise computations are used to identify and understand significant trends in peak sound amplitudes and radiation angles. The peak sound radiation angles are explained well with the Mach wave model of Tam & Tanna (*J. Sound Vib.* Vol. 81, 1982, p. 337). The observed reduction of peak sound amplitudes with frequency correlates well with the corresponding reduction of instability wave growth with frequency. However, in order to account for variation of sound amplitude for different azimuthal modes, the radial structure of the instability waves must be considered in addition to streamwise growth. The effect of heating on the $M_j = 1.22$ jet is shown to enhance the sound radiated due to the axisymmetric instability waves while the other modes are relatively unaffected. Solutions to a Lilley–Goldstein equation show that sound generated by 'thermodynamic' source terms is small relative to sound from 'momentum' sources though heating does increase the relative importance of the thermodynamic source. Furthermore, heating preferentially amplifies sound associated with the axisymmetric modes owing to constructive interference between sound from the momentum and thermodynamic sources. However, higher modes show destructive interference between these two sources and are relatively unaffected by heating.

1. Introduction

Modern airplane jet engines often operate at off-design conditions where the engine exhaust velocity is supersonic, and a 'mismatch' exists between the flow and ambient pressures. In such cases, a quasi-steady pattern of shock-waves forms in the interior of the exhaust flow, and the interaction between jet turbulence and these shock-waves

produces what is often referred to as 'shock-noise'. Depending on the flow conditions, shock-noise may be a significant component of the overall jet noise. In this study, numerical solutions to a model problem are used to gain insight into the generation and radiation of (broadband) shock-noise. Specifically, coherent structures in supersonic turbulent jets are modelled as linear instability waves, and we consider the sound generated by the interaction between these instability waves and the shock-cell structure.

In addition to broadband shock-noise, supersonic jets produce two other types of noise: (i) mixing noise and (ii) screech tones which we now briefly summarize. Mixing noise is generated directly by the turbulent fluctuations in the jet. The study of mixing noise extends back to the seminal work of Lighthill (1952), and it is still an active area of research. Screech tones are generated by 'resonant' interactions involving turbulent eddies, shock-waves and shock-noise. The basic mechanism of screech generation was expounded by Powell (1953), and since then numerous theoretical, experimental and computational studies have led to an increased understanding of this phenomenon. See Raman (1999) for a review.

A review of supersonic jet noise and its three components is given by Tam (1995), and a review of computational aeroacoustics is given by Colonius & Lele (2004). We now narrow our focus to shock-noise. The first comprehensive study of broadband shock-noise was conducted by Harper-Bourne & Fisher (1973). They identified many significant features of shock-noise based on their experimental measurements. Perhaps the most notable of these was the observation that the shock-noise intensity for jets emitted from conical nozzles scaled as β^4, where $\beta^2 = M_j^2 - 1$ and M_j is the 'fully-expanded' jet Mach number which is based on the jet velocity, U_j, and speed of sound, a_j. Drawing upon their measurements and physical reasoning, Harper-Bourne & Fisher (1973) proposed a model which approximated the shock-noise sources as a series of point sources located at shock–turbulence interaction locations. Of particular importance was the observation that if the turbulence maintained its coherence as it convected through multiple shock-cells, positive interference from the sources would result in strong radiation in the upstream direction. Specifically, the predicted (and observed) peak frequency was given by

$$f_p = \frac{U_c}{L(1 - M_c\cos(\psi))}, \tag{1.1}$$

where f_p is the peak frequency, U_c is an appropriate convection velocity, L is the shock-cell spacing, M_c is the convective Mach number, and ψ is the observation angle measured relative to the downstream-directed jet axis. A general prediction method for the sound spectra was also developed. A 'source spectral density' and correlation coefficients were required as input and obtained from experiment. Harper-Bourne & Fisher showed that predictions obtained from this model agreed with measurements for a $M_j = 1.41$ jet.

Howe & Ffowcs Williams (1978) developed a theoretical shock-noise model where the jet turbulence was represented by convecting axisymmetric vortex rings and an acoustic analogy approach was used to obtain the sound field. Experiments by Tanna (1977) provided further insight into the characteristics of shock-noise while illustrating that the Harper-Bourne & Fisher (1973) model worked well over a broad range of jet conditions. The experimental study of Norum & Seiner (1982*a*) showed that a frequency scaled with the ambient speed of sound (rather than jet velocity) gave the best correlation for the peak shock-noise frequency. They also used

a source-localization technique to determine that the source location for a highly under-expanded jet occurred between the sixth and tenth shock-cells.

Tam & Tanna (1982) provided a different perspective on the problem by modelling turbulent eddies as instability waves. With this model, it was argued that shock-noise should radiate strongly at upstream angles as Mach waves, and a frequency–directivity relation equivalent to (1.1) was derived. They also generalized the Harper-Bourne & Fisher (1973) β^4 intensity scaling to converging–diverging nozzles. Tam (1987, 1990, 1991) built upon the approach of Tam & Tanna and developed a semi-empirical shock-noise model which showed good agreement with experiment. Specifically, Tam (1987) posed the problem as computing sound generated by the weakly nonlinear interaction between linear instability waves and the shock-cell structure. He did not compute direct solutions to this problem. Rather, he developed an approximate semi-empirical solution using physical reasoning, scaling arguments and empirical fits to experimental measurements.

There are several other works which are relevant to the shock-noise problem, and the introduction of Lui (2003) gives a thorough overview of the literature.

The models of both Harper-Bourne & Fisher (1973) and Tam (1987) rely on empirical results to model the jet turbulence. The Harper-Bourne & Fisher (1973) representation of turbulence temporal dynamics is more sophisticated than the linear stability model of Tam, and thus leads to a more substantial dependence on experiment. However, this dependence is reduced through the use of scaling relations and modelling simplifications which lead to a 'universal source' spectrum. The instability wave model cannot produce sound spectra that are as 'realistic' as the Harper-Bourne & Fisher (1973) model, but it does provide a path for more direct calculations of the shock-noise problem.

In this work, we adopt Tam's (1987) formulation and compute sound generated by instability wave/shock-cell interaction. This approach requires the construction of shock-noise sources and the calculation of the sound generated by these sources. The computational results are used to understand how and why the source and sound fields are modified as frequency, azimuthal mode number and jet conditions are varied.

The next section reviews basic features of shock-noise in the context of a simple model problem. Then, we present the governing equations, the numerical methods used to solve these equations, and a test problem. This is followed by a survey of the linear stability computations that have been performed. Section 5 is the core of this paper; there, the results of shock-noise computations are presented and analysed. Trends in peak radiation angles and amplitudes are explained and connections between the instability waves, shock structure, sound sources and shock-noise are elucidated.

2. Background

A few basic features of shock-noise can be understood by examining a simple model problem. Borrowing from Tam & Tanna (1982) and Tam (1987), we consider a source which is the product of a propagating wave with a Gaussian envelope (approximating an instability wave), $h^{(t)}$, and a neutral steady wave (approximating a mode of the shock structure), $g^{(s)}$:

$$f(x, r, t) = h^{(t)} g^{(s)}, \tag{2.1a}$$

$$h^{(t)} = A(r) \exp(\mathrm{i}(k_t x - \omega_0 t)) \exp(-4 \ln(2)(x/L)^2), \tag{2.1b}$$

$$g^{(s)} = B(r) \left[\exp(\mathrm{i}k_s x) + \exp(-\mathrm{i}k_s x)\right], \tag{2.1c}$$

where x and r are the streamwise and transverse directions, respectively. A and B are arbitrary functions representing the radial dependence of the source components; their influence is ignored in the discussion which follows. The far-field pressure takes the following form:

$$p \sim C(\psi)\frac{\exp(\mathrm{i}(\omega_0 R - \omega_0 t))}{\pi R}\sqrt{\frac{\pi L^2}{4\ln(2)}}\left\{\exp\left(-\frac{(k_1^* L)^2}{16\ln(2)}[1 - c_{s1}\cos(\psi)]^2\right) + \exp\left(-\frac{(k_2^* L)^2}{16\ln(2)}[1 - c_{s2}\cos(\psi)]^2\right)\right\}, \quad (2.2a)$$

$$k_1^* = k_t - k_s; \qquad k_2^* = k_t + k_s, \quad (2.2b)$$

$$c_{s,j} = \frac{\omega_0}{k_j^*}. \quad (2.2c)$$

(All equations/parameters in this paper are non-dimensionalized with the fully expanded jet diameter, D, ambient density, ρ_∞, and the ambient speed of sound, a_∞, unless noted otherwise.) Equation (2.2) is in spherical coordinates, (R, ψ, ϕ), with ψ measured from the downstream-oriented jet axis, and $C(\psi)$ is included to account for the arbitrary radial structure of the source and mean-flow effects. The 'antenna' terms of the form $\exp(-((k_j^* L)^2/16\ln(2))[1 - c_{s,j}\cos(\psi)]^2)$ are of primary interest. If the 'source phase velocity,' $c_{s,j}$, is supersonic with respect to the ambient speed of sound ($|c_{s,j}| > 1$), there is intense sound radiation at angles near the Mach angle, $\psi_{M,j} = \cos^{-1}(1/c_{s,j})$. However, for the shock-noise problem, $c_{s,2}$ is generally subsonic. Furthermore, this term radiates sound primarily in the downstream direction where shock-noise is not significant when compared to the mixing noise. So, it is the k_1^* term which is important, and the formula for $\psi_{M,1}$ corresponds to the peak frequency equation, (1.1). Thus, we have arrived at a significant conclusion from Tam & Tanna: 'Sound due to shock-cell/instability wave interaction can take the form of Mach wave radiation at an effective Mach angle defined by the instability wave frequency and the difference between the instability wave and shock-cell mode wavenumbers.'

The final point of interest is the effect of the frequency on the directivity of the sound. We can quantify this effect by using the semi-empirical models for the Gaussian envelope, instability wavenumber and shock-cell wavelengths developed by Tam (1987). Based on scaling arguments and fits to experimental data for the resulting sound spectra, Tam arrived at the following function for the half-width:

$$L = \frac{M_j(T_j/T_\infty)^{(1/2)}}{\omega}\left[\alpha + \beta M_j^2 + \gamma T_j/T_\infty\right], \quad (2.3)$$

where α, β and γ are empirical constants. Tam modelled the instability wavenumber as $k_t = \omega/0.7U_j$ and used a modified vortex sheet solution for k_s:

$$k_{s,1} = (1.596 - 0.1773M_j)k_{s,1,\textit{vortex sheet}}, \quad (2.4a)$$

$$k_{s,2} = 1.1k_{s,2,\textit{vortex sheet}}, \quad (2.4b)$$

$$k_{s,m} = k_{s,m,\textit{vortex sheet}}, m = 3, 4, \ldots, \quad (2.4c)$$

where k_{sm} is the mth shock-cell mode. Figure 1 shows the antenna function, $\exp(-((k_1^* L)^2/16\ln(2))[1 - c_{s,1}\cos(\psi)]^2)$, for an $M_j = 1.2$, unheated jet with frequencies $St = 0.6$ and $St = 0.9$. The Strouhal number is defined as $St = \omega_0 D/2\pi U_j$. Tam's model is used to determine k_t and $k_{s,1}$. As the frequency increases, the sound peak shifts

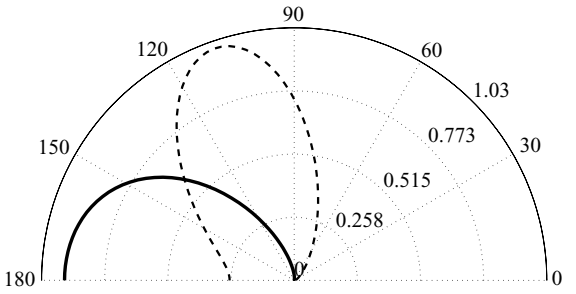

FIGURE 1. The effect of frequency on antenna function for the shock-cell mode/instability wave interaction model problem. Flow parameters are for a $M_j = 1.2$ unheated jet; ——, $St = 0.6$; - - -, $St = 0.9$.

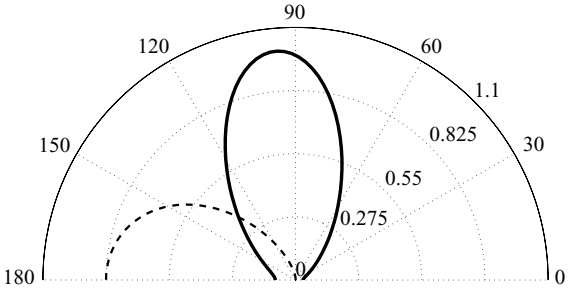

FIGURE 2. The influence of higher shock-cell modes at higher frequencies on the antenna function for the shock-cell mode/instability wave interaction model problem. Flow parameters are for a $M_j = 1.2$ unheated jet; $St = 1.05$; ——, 1st shock mode; - - -, 2nd shock mode.

towards the downstream direction while the lobe width remains approximately the same. If the frequency is increased further, the directivity will shift to larger inlet angles, and eventually the shock-noise will be insignificant relative to the mixing noise. Figure 2 shows directivities for $St = 1.05$ representing instability wave interaction with both the first ($k_{s,1}$) and second ($k_{s,2}$) shock-cell modes. As demonstrated in the figure, higher shock modes can make significant contributions to the sound at higher frequencies and small inlet angles. This model problem illustrates many of the qualitative aspects of shock-noise, and Tam (1987), using a moderately more sophisticated approach, was able to obtain good quantitative results for sound spectra. Later in this work, we explicitly compute the source terms and the resulting sound without using the similarity assumptions and semi-empirical relations of Tam (1987). This approach will allow us to study the nature of shock-noise generation and radiation in much greater depth than existing models allow. Of course, the direct applicability of our results is limited by modelling assumptions, so we will focus on the qualitative features of the problem.

3. Formulation and methodology

We adopt a cylindrical coordinate system (x, r, ϕ) where the x-axis and jet axis are the same. We will consider small-amplitude disturbances (shock-cells, instability waves and shock-noise) on axisymmetric mean flows. The disturbances are expanded as Fourier series in the azimuthal direction with mode number, m, and computations are performed on $x-r$ grids for each mode number of interest. We generally focus on

the pressure asymptotically far from the jet nozzle in spherical coordinates (R, ψ, ϕ) where $x = R\cos(\psi)$, $r = R\sin(\psi)$. We refer to this pressure as the 'far-field sound' which, for a given azimuthal mode, m, and frequency, ω, is defined as:

$$p_{ff} \equiv |\lim_{\omega R \to \infty} p_m(R, \psi)|R. \tag{3.1}$$

The far-field sound will usually be presented in terms of the 'inlet angle', $\theta = 180 - \psi$.

3.1. *Governing equations*

Following Tam (1987), shock-noise is modelled as the product of a weakly nonlinear interaction between linear instability waves and the shock-cell structure. Specifically, we decompose the flow variables into:

$$f = \overline{F} + f^t + f^s + f' + f^{other}, \tag{3.2}$$

where $\overline{F}$ is the steady specified (perfectly expanded) mean flow, f^t represents instability waves, f^s is the shock-cell structure, f' is the sound generated by the interaction between f^t and f^s, and f^{other} is defined to account for unrelated and higher-order nonlinear terms. Assuming that f' is small, and neglecting dissipative effects in sound generation and propagation, we define the shock-noise as a solution to the inhomogeneous linearized Euler equations:

$$\frac{\partial \rho'}{\partial t} + \frac{\partial m_j'}{\partial x_j} = S_\rho, \tag{3.3a}$$

$$\frac{\partial m_i'}{\partial t} + \frac{\partial}{\partial x_j}(m_i'\overline{U_j} + m_j'\overline{U_i} - \rho'\overline{U_i}\,\overline{U_j}) + \frac{\partial p'}{\partial x_i} = S_{m,i}, \tag{3.3b}$$

$$\frac{\partial e'}{\partial t} + \frac{\partial}{\partial x_j}[u_j'(\overline{E} + \overline{P}) + \overline{U}_j(e' + p')] = S_e, \tag{3.3c}$$

$$S_\rho = -\frac{\partial}{\partial x_j}\left[\rho^{(t)}u_j^{(s)} + \rho^{(s)}u_j^{(t)}\right], \tag{3.4a}$$

$$S_{m,i} = -\frac{\partial}{\partial t}\left[\rho^{(t)}u_i^{(s)} + \rho^{(s)}u_i^{(t)}\right] - \frac{\partial}{\partial x_j}\left[m_j^{(t)}u_i^{(s)} + m_j^{(s)}u_i^{(t)} + \left(\rho^{(t)}u_j^{(s)} + \rho^{(s)}u_j^{(t)}\right)\overline{U_i}\right], \tag{3.4b}$$

$$S_e = -\frac{\partial}{\partial t}\left[\overline{U}_j\left(\rho^{(t)}u_j^{(s)} + \rho^{(s)}u_j^{(t)}\right) + \overline{\rho}u_j^{(t)}u_j^{(s)}\right] - \frac{\partial}{\partial x_j}\left[u_j^{(t)}\left(e^{(s)} + p^{(s)}\right) + u_j^{(s)}\left(e^{(t)} + p^{(t)}\right)\right]. \tag{3.4c}$$

In (3.3) and (3.4), u_i' is the velocity disturbance, ρ' is the density disturbance, p' is the pressure disturbance, $m_i' \equiv \rho'\overline{U_i} + \overline{\rho}u_i'$ is the momentum disturbance, and e' is the total energy disturbance. A perfect gas equation of state closes the system of equations,

$$e' = \frac{p'}{\gamma - 1} + \overline{\rho}(\overline{U_j}u_j') + \tfrac{1}{2}\rho'(\overline{U_j}\,\overline{U_j}). \tag{3.5}$$

The shock-cell modes are taken to be axisymmetric and stationary. Thus, the frequency and azimuthal mode number of an instability wave sets the frequency and mode number of both the shock-noise sources (3.4) and the resulting sound.

Both the shock-cell structure and instability waves are computed as small disturbances on the perfectly expanded mean flow. The perfectly expanded mean flow is computed by solving RANS equations with the modified $k-\epsilon$ model of Thies & Tam (1996). The instability waves, which represent coherent structures in the fully turbulent flow, are defined as solutions to the linear parabolized stability

equations (PSE). The shock-cell structure is determined by solving the locally-parallel 'quasi-viscous' linear stability equations following Tam, Jackson & Seiner (1985). A clear shortcoming of this formulation is that the effect of the shock structure on the evolution of the instability waves is neglected. This effect may be significant for higher-frequency instability waves and for larger nozzle pressure ratios. Also, as frequency is increased, disturbances are expected to become less coherent, and an instability wave representation becomes less appropriate. For these reasons, we constrain ourselves to shock-noise frequencies which are less than $St \sim 1.0$.

In the following sections, we outline the methods used for the RANS, PSE, shock-cell and LEE computations. Then, details of the shock-noise computations and a test problem are presented. The full governing equations as well as several validation cases can be found in Ray (2006).

3.2. *Mean flow computation*

The spreading mean flows used in the LEE and stability computations in this work were obtained by solving the steady, axisymmetric, compressible boundary-layer equations with modified $k-\epsilon$ equations (Wilcox 1993; Thies & Tam 1996). The Thies model has been calibrated to provide good predictions of cold jet spreading rates over a Mach number range of $\sim 0.4-2.2$ which makes it well suited for our ($M_j = 1.22$ and $M_j = 1.36$) shock-noise computations.

Second-order central differences are used for the radial derivatives, and a mapping function clusters points in the shear layer. The solution is marched in the x-direction with a second-order (Adams–Bashforth) forward difference. At each x position, the solution is iterated until the maximum difference for each dependent variable between iterations is less than some tolerance (usually 10^{-12}). Linearization (with respect to iteration) at iteration level k is implemented as:

$$\overline{\rho}\overline{U}_j \frac{\partial \overline{U}_i}{\partial x_j} = (\overline{\rho}\overline{U}_j)^{k-1} \frac{\partial \overline{U}_i{}^k}{\partial x_j}. \tag{3.6}$$

While more sophisticated iterative schemes will lead to faster convergence, we find that this method is sufficiently efficient for our needs. An initialization process has been implemented with two goals in mind: (i) to remove the influence of 'transients' associated with the choice of the initial profile, and (ii) to maintain the good agreement with experiment obtained in the calculations of Thies & Tam (1996). A result of this process is an 'initialization region' from $x \sim -1.6$ to $x = 0$ over which the initially laminar shear-layer spreading rate increases to its turbulent value. At the 'nozzle location', $x = 0$, the momentum thickness (see (3.7)) is $\delta^I/D \sim 0.03$. (There is no physical nozzle in our computations; we normalize the instability waves and shock-cell disturbances assuming that there is a nozzle at $x = 0$.) The mean flow solution in the initialization region, $x < 0$, is retained and used to initialize the shock-cell and instability wave computations.

We use two forms of the momentum thickness to describe the jet development. The first is the 'incompressible planar' momentum thickness defined as

$$\delta^I = \int_0^\infty \frac{\overline{U}-\overline{U}_\infty}{\overline{U}_{cl}-\overline{U}_\infty}\left(1-\frac{\overline{U}-\overline{U}_\infty}{\overline{U}_{cl}-\overline{U}_\infty}\right)\mathrm{d}r. \tag{3.7}$$

We also use the conventional momentum thickness,

$$\delta = \int_0^\infty \frac{\overline{\rho}}{\overline{\rho}_{cl}}\frac{\overline{U}-\overline{U}_\infty}{\overline{U}_{cl}-\overline{U}_\infty}\left(1-\frac{\overline{U}-\overline{U}_\infty}{\overline{U}_{cl}-\overline{U}_\infty}\right)r\,\mathrm{d}r. \tag{3.8}$$

3.3. *Shock-cell computations*

The shock-cell disturbances are obtained by solving linear locally-parallel quasi-viscous stability equations. They are quasi-viscous in the sense that viscous and heat-conduction terms in the energy equation are neglected. This approach is taken directly from Tam *et al.* (1985). A simple eddy-viscosity model is used to account for shock-cell decay due to turbulent diffusion. A radially constant eddy viscosity is specified based on a constant local Reynolds number, $U_{cl}\delta^I/\nu_t = 95$. Tam *et al.* (1985) show that this model gives good agreement with the shock-cell pressure measurements of Norum & Seiner (1982*b*) over a broad range of flow conditions. The equations are solved at each streamwise position with a shooting method that uses the re-orthonormalization procedure of Conte (1966).

3.4. *Instability wave computation*

The linear PSE can be derived by first linearizing the compressible Navier–Stokes equations about a base flow, $\overline{f}$, and assuming solutions of the form:

$$f(x, r, \phi, t) = \tilde{f}(r, x)\exp\{\mathrm{i}[\Phi(x) + m\phi - \omega t]\}. \tag{3.9}$$

Here, m and ω must be specified while the shape function, $\tilde{f}$, and phase, Φ are unknowns. Applying the slowly varying or 'parabolizing' assumption (e.g. Herbert 1997),

$$\frac{\partial^2 \tilde{f}}{\partial x^2} \sim 0, \qquad \frac{1}{Re}\frac{\partial \tilde{f}}{\partial x} \sim 0, \qquad \frac{\partial^2 \overline{f}}{\partial x^2} \sim 0, \qquad \frac{1}{Re}\frac{\partial \overline{f}}{\partial x} \sim 0, \tag{3.10}$$

we arrive at the final equations which are of the form:

$$\boldsymbol{L}_0\Psi + \boldsymbol{L}_1\frac{\partial \Psi}{\partial r} + \boldsymbol{L}_2\frac{\partial^2 \Psi}{\partial r^2} + \boldsymbol{M}\frac{\partial \Psi}{\partial x} = 0. \tag{3.11a}$$

$$\Psi = [\tilde{\rho}\ \tilde{u}_x\ \tilde{u}_r\ \tilde{u}_\theta\ \tilde{T}]^T, \tag{3.11b}$$

where $\tilde{\rho}$, $\tilde{u}_x$, $\tilde{u}_r$, $\tilde{u}_\theta$ and $\tilde{T}$ are the shape functions for density, streamwise velocity, radial velocity, azimuthal velocity and temperature, respectively. Full expressions for the matrices, $\boldsymbol{L}_0$, $\boldsymbol{L}_1$, $\boldsymbol{L}_2$, $\boldsymbol{M}$ can be found in Ray (2006). The PSE system also contains an eigenvalue, $\alpha = \mathrm{d}\Phi/\mathrm{d}x$.

Equation (3.11*a*) is marched downstream using a first-order implicit method in x and fourth-order central differences in r. A grid-mapping is used to cluster points in the shear layer. At each streamwise step, a discrete solution is sought which satisfies a normalization condition:

$$\int_0^{r_{max}} \overline{\rho}\left(\tilde{u}_j^*\frac{\partial \tilde{u}_j}{\partial x}\right)\mathrm{d}r = 0. \tag{3.12}$$

The normalization sets the distribution of energy between the shape function and complex exponential in (3.9). Comparisons with computations which used the 'compressible' norm used by Hanifi, Schmid & Henningson (1996) indicate that the full solution is practically insensitive to the choice of normalization function. The eddy-viscosity model used in the shock-cell computations is used here as well with $Re_t \equiv U_{cl}\delta^I/\nu_t = 600$. This value is roughly one order of magnitude larger than the peak eddy viscosity used in the RANS computations which is in basic agreement with the expectation that large-scale coherent disturbances exert a greater influence on mean-flow spreading than small-scale incoherent motions. Increasing the eddy viscosity reduces instability wave growth and shifts the amplitude peak towards the nozzle. Tests indicate that the phase velocity is insensitive to changes in Re_t (see Ray

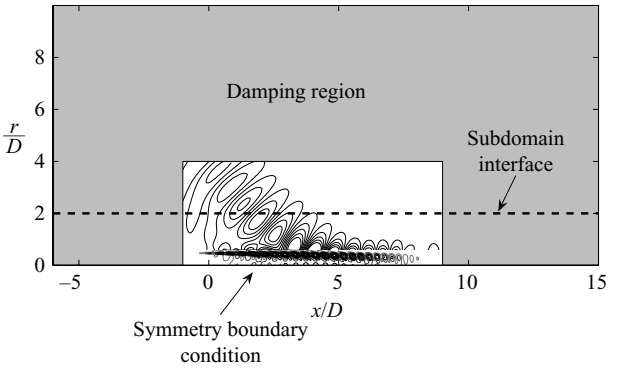

FIGURE 3. Schematic of the LEE computational domain.

2006, for a discussion of the effect of Re_t on computed solutions). Apart from the use of an eddy viscosity model, the PSE methodology used here similar to those used in earlier studies which considered the linear stability of compressible free shear layers (e.g. Balakumar 1998; Yen & Messersmith 1999; Malik & Chang 2000; Cheung & Lele 2004).

PSE computations of flows which are not supersonic in the entire domain exhibit numerical instability if the streamwise step size is 'too small'. We have used the rule, $\Delta x > 1/\mathrm{Re}\{\alpha\}$ (Li & Malik 1994), to guide our selection of step size. Aside from this difficulty, the PSE approach appears to be well-suited for computing the convective instabilities considered in this study (see pp. 253–254 of Herbert 1997, and references therein for discussions on the validity and applicability of the PSE method).

The PSE solutions are computed on RANS mean flows which extend 1.6 diameters upstream of the nominal nozzle location. The initialization procedure consists of three stages. First, the inviscid parallel instability solution is obtained at the first streamwise station, $x = -1.6$. Then, the full PSE equations are solved over 1.6 diameters with the same initial velocity profile. This step removes transients associated with the inviscid parallel solution. The final stage of the initialization starts at $x = -1.6$ with the solution from the previous stage and solves the full PSE equations up to $x = 0$. After initialization, the PSE are solved for $x > 0$ with the RANS mean flow. When forming source terms for the LEE equations, the solution from the third initialization stage is retained.

3.5. *Numerical method for solution of linearized Euler equations*

An explicit time-marching pseudospectral multidomain code has been developed to solve (3.3). The two-step fourth-order low-dissipation low-dispersion low-storage Runge–Kutta scheme of Stanescu & Habashi (1998) (see also Hu, Hussaini & Manthey 1996) is used for time advancement. (Solution of the LEE in the frequency domain is a viable alternative. We chose to use a time domain approach for two reasons: (i) several frequencies can be solved simultaneously and (ii) the same numerical approach can be used for problems with non-harmonic sources, if desired.) The overall computational domain is split into subdomains, and within each subdomain, spatial derivatives are calculated with Chebyshev transforms. Along the boundaries, damping layers and non-reflecting boundary conditions are implemented as shown in figure 3. To compute the far-field sound from the LEE solution, the following steps are taken:

(*a*) The time history of pressure is collected along the cylindrical surface, $r = r_0$, where r_0 lies far enough above the shear layer to neglect the effects of the radial mean flow and mean flow gradients.

(*b*) The pressure signal is Fourier transformed in time and the component corresponding to the forcing frequency is extracted.

(*c*) The pressure is then Fourier transformed in the streamwise direction (the Fourier transforms are defined in equation (B 1*b*)) and matched to an appropriate solution of the wave equation (a Hankel function).

(*d*) The inverse Fourier transform in the streamwise direction is computed with the method of stationary phase giving the far-field sound.

A spectral exponential filter (Majda, McDonough & Osher 1978; Gottlieb & Hesthaven 2001) is applied in the streamwise and radial directions at each time substep of the LEE computation. Damping layers are applied at the inflow, outflow and top of the computational domain to reduce spurious reflection. The computational grid (in both x and r) consists of the Gauss–Lobatto points. These points are clustered near the domain boundaries. However, for the shock-noise problems of interest, the greatest demands on resolution are expected to occur in the shear layer and away from the radial and streamwise boundaries (there are damping layers at the streamwise boundaries which make near-boundary clustering particularly undesirable). For these reasons, we have used two mapping functions to map the computational (Gauss–Lobatto) grid to a physical grid with a more efficient distribution of points. One must be careful, however, when using mappings with Chebyshev methods; if some clustering near the boundaries is not retained, the accuracy of the Chebyshev representation deteriorates. For the inner subdomain, we use the Bayliss & Turkel (1992) mapping for the radial direction. The Kosloff & Tal-ezer (1993) mapping is used for the outer subdomain radial mapping and streamwise mapping. 'Information' is transferred between the subdomains using characteristics-based patching at the subdomain interface following Hesthaven (1997). See Appendix A for further details on the numerical method.

3.6. *Instability wave/shock-cell interaction: computational setup and a test case*

The instability wave/shock-cell interaction problem requires the assembly of nonlinear source terms (figure 4). We now present details of this assembly procedure and then proceed to a test problem. In general, the RANS mean flow is computed on two different x-grids – the non-uniform grid used by the LEE solver (at $x = -1, 5, 11$, the step sizes are $\Delta x = 0.050, 0.053, 0.048$ – see Appendix A for further details on the LEE grids) and the uniform grid used by the PSE code. A streamwise step size of $0.025D$ is used in the PSE computations for $St \geqslant 0.6$, and $0.05D$ is used for $St < 0.6$. For all computations presented here, the radial domain is 10 diameters. The RANS code uses 1600 grid points in the radial direction and the PSE code uses 400 points (a grid mapping clusters points in and around the shear layer). Since the RANS, PSE and LEE radial grids are all different (the shock-cell disturbances are solved directly on the LEE grid), the RANS data must be interpolated to the PSE and LEE grids, and the PSE solution must be interpolated to the LEE grid. Interpolation of the RANS results is a two-stage process. Cubic spline interpolation gives the mean flow on the LEE grid. A spectral filter is then applied to smooth the front which the $k - \epsilon$ model produces at the inner edge of the shear layer. This is simply a 'safety' measure and has little effect on the gross mean flow properties or the shock-noise.

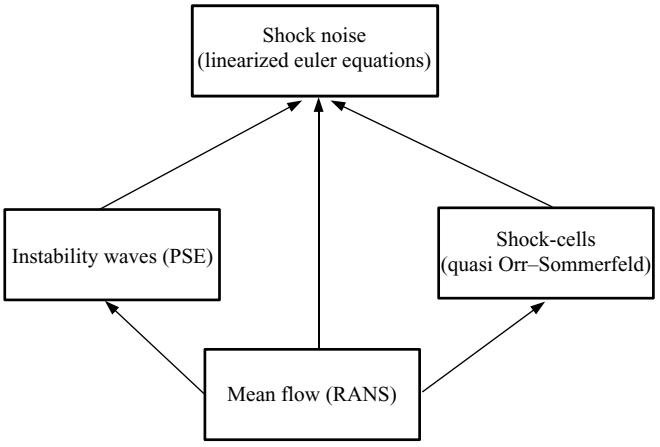

FIGURE 4. Overview of methods for instability wave/shock-cell interaction computations.

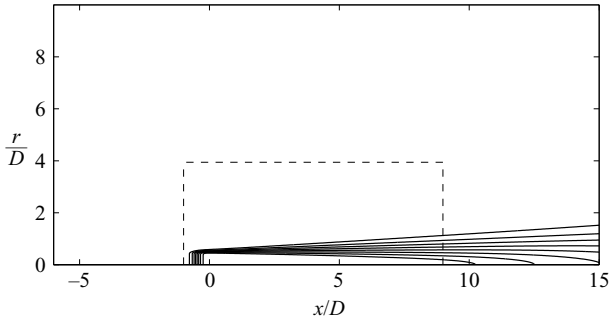

FIGURE 5. Contours of mean streamwise velocity for the $M_j = 1.22$ cold jet.

After filtering, the mean flow is spectrally interpolated onto the PSE grid. Cubic spline interpolation is used to interpolate the PSE solution onto the LEE grid.

The LEE domain for shock-noise computations extends several diameters upstream of the nominal nozzle location so smooth specifications of the mean flow, shock-cells, and instability waves are required in this region. The mean flow computation starts at $x \sim -1.6$ and the flow is extended upstream with a parallel flow assumption and damped to ambient conditions with a tanh function,

$$\overline{U}_{x,LEE} = \overline{U}_{x,RANS} - (\overline{U}_{x,RANS} - M_\infty)\left(\tfrac{1}{2}(1 - \tanh(4(x + 0.5)))\right). \tag{3.13}$$

Contours of the mean axial velocity used by the LEE code for the $M_j = 1.22$ cold jet are shown in figure 5. Physically, the shock structure should start at $x = 0$ and be zero upstream of this point. However, including this strong discontinuity places an extreme burden on the numerical method, so the shock structure is damped in a manner similar to the mean flow. The solution is extended upstream of $x = -1.6$ (recall that both the shock-cell and PSE computations begin at $x \sim -1.6$) with a neutral stability assumption and rapidly damped upstream of $x = 0$ with a damping function similar to the one used for the mean flow,

$$f_{sc,LEE} = f_{sc}\left\{\tfrac{1}{2}(1 + \tanh[4(x + 0.5)])\right\}. \tag{3.14}$$

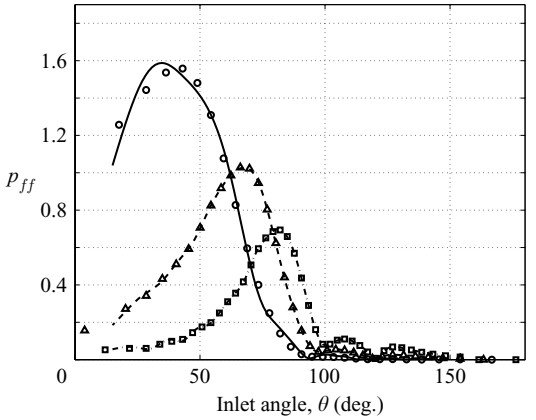

FIGURE 6. Shock-noise test case, $M_j = 1.22, m = 0$. Curves correspond to LEE solutions and symbols represent Rayleigh equation solutions. ——, $St = 0.6$ (LEE); - - -, $St = 0.75$ (LEE); –.–, $St = 0.9$ (LEE).

The upstream extension of the PSE solution is implemented by taking the shape function and eigenvalue for $x < -1.6$ to be equal to their values at $x = -1.6$. Thus, the growth rate at $x = -1.6$ determines the rate at which the instability wave decays as it is extended from $x = -1.6$ to $x = -6.0$. At $x = -1.6$, the shear layer is thin, and the growth rate is large, so, the upstream extension of the instability wave decays away quickly. We normalize all instability waves used in shock-noise computations so that the integrated disturbance kinetic energy at $x = 0$ is one.

All computations were performed on a linux cluster consisting of 24 AMD Opteron (1.6 GHz) processors. Single-processor mean flow and shock-mode calculations typically required 10–15 min and 2–3 h, respectively. PSE calculations for a single azimuthal mode and several frequencies were carried out in parallel with one frequency per processor. Typical calculations required 4–5 h. LEE calculations were carried out on 8 processors and a computation of an azimuthal mode required 2–4 days, though the coarse-grid approach discussed in § 5.2.2 reduces this time considerably.

We have undertaken several validation problems to verify that the LEE code performs well for acoustic source problems (Ray 2006). Here, we will present just one of these tests – a problem which is very similar to the full shock-noise problem. The full problem is given by (3.3) and (3.4) with a spreading axisymmetric base flow. If we replace the base flow on the left-hand side of (3.3) with a parallel (tanh) base flow, the equations can be reduced to the inhomogeneous Rayleigh equation (see Appendix B). We can then compare LEE and Rayleigh solutions which will simultaneously test the LEE and Rayleigh codes. RANS mean flows, PSE-generated instability waves, and the first shock-cell mode go into the right-hand sides of the equations. The only neglected effect is the effect of mean flow spreading on the sound radiation. Most of the numerical parameters used in both these tests and the full shock-noise computations presented later have been included in Appendix A.

The test case is a $M_j = 1.22$ cold jet with shock-noise sources containing axisymmetric ($m = 0$) instability waves at frequencies $St = 0.6, 0.75, 0.9$. Figure 6 shows the far-field pressure amplitudes. Agreement between solution methods is very good; however, there is some error for the $St = 0.6$ case at shallow angles. In this and other test cases not shown here, deficiencies in the far-field sound computation method

M_d	M_j	$\frac{U_j}{a_\infty}$	$\frac{T_j}{T_\infty}$	$\frac{T_r}{T_\infty}$	St	$\frac{\omega D}{a_\infty}$
1.00	1.22	1.07	0.77	1.00	0.60, 0.75, 0.90	4.04, 5.05, 6.06
1.00	1.22	1.59	1.70	2.20	0.60, 0.75, 0.90	5.99, 7.49, 8.98
1.50	1.36	1.19	0.77	1.05	0.54, 0.67, 0.81	4.04, 5.05, 6.06

TABLE 1. Flow and source parameters for shock-noise computations. M_d is the 'design Mach number' (the jet Mach number at the nozzle exit). T_j and T_r are the jet static and stagnation temperatures, respectively.

produce tangible errors at shallow inlet angles. For this reason, in the discussion of shock-noise that follows, only sound radiated at angles $30 < \theta < 150$ will be considered.

The shock-noise sources also excite instability waves which propagate downstream. These waves will generate sound directly. However, this sound (which is also a type of 'shock-noise') will tend to radiate at shallow downstream angles, and it is not expected to be significant relative to the shock-noise at normal and upstream angles. The test case provides a partial validation of this expectation – the LEE result contains sound associated with excited instability waves while the Rayleigh equation solution does not.

4. Results: mean flow, shock-cells and instability waves

4.1. *Overview of computations*

Computations for three flows will be discussed. We take an $M_j = 1.22$, $M_d = 1.0$ cold jet as a 'base case'. The two other flows are higher Mach number (same temperature ratio as base case) and heated (same Mach number as base case). Furthermore, the higher-Mach-number case is over-expanded with $M_d = 1.5$. The Mach numbers for the over-expanded case were chosen primarily to satisfy two criteria: (i) the pressure mismatch should be sufficiently small to justify the linear shock-cell assumption, and (ii) the jet Mach number should be be fairly close to the base case Mach number. The second condition was applied because a large difference in jet Mach numbers would have required modifications to the mean flow initialization procedure and computational domain size – complications which we wished to avoid. Each flow also contained a small free-stream velocity, $M_\infty = 0.01$.

For each flow, three azimuthal mode numbers ($m = 0, m = 1, m = 2$) are solved and three frequencies per azimuthal mode number are computed. The frequencies for the two $M_j = 1.22$ jets are $St = 0.6, 0.75, 0.9$. The acoustic frequencies of the base and $M_j = 1.36$ cases are the same, $\omega D/a_\infty = 4.04, 5.05, 6.06$. Experiments indicate that broadband shock-noise is significant at these frequencies. A single computation consists of all frequencies at a single azimuthal mode number, so nine computations were required for these three flows. An overview of the flow parameters is given in table 1. Before examining the shock-noise results, we first briefly summarize the mean flow and shock-structure computations, and examine pertinent characteristics of the linear instability waves.

4.2. *Mean flow and shock-structure*

The centreline axial velocities and momentum thicknesses for the three RANS-computed mean flows are shown in figure 7. We see that the $M_j = 1.36$ jet spreads at a slightly slower rate than the base case, illustrating the effect of compressibility. The

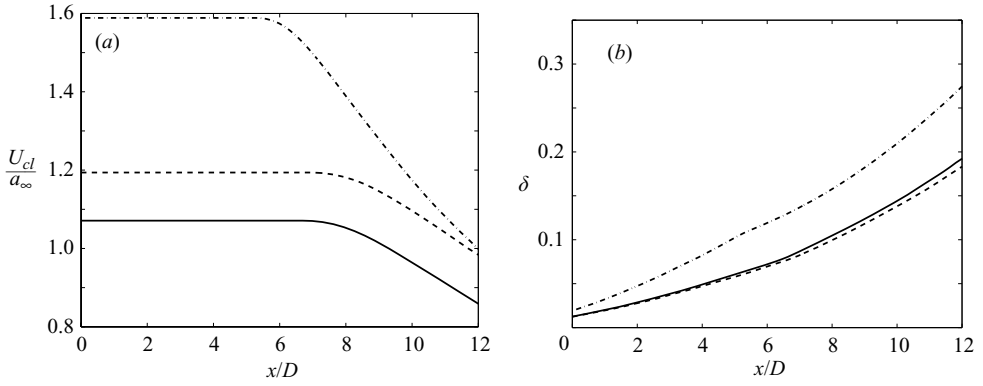

FIGURE 7. Mean flow (*a*) centreline velocities and (*b*) momentum thicknesses, δ. ——, $M_j = 1.22$, cold; - - -, $M_j = 1.36$, cold; -.-, $M_j = 1.22$, hot.

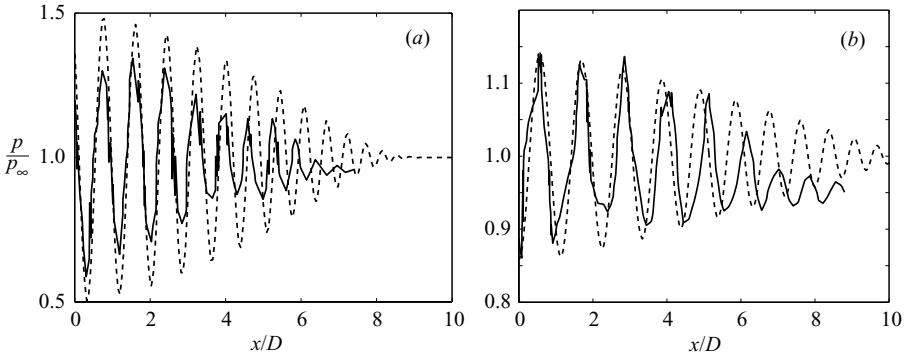

FIGURE 8. Shock-cell pressure, (*a*) $M_j = 1.22$, $M_d = 1.0$, $r/D = 0$ (*b*) $M_j = 1.36$, $M_d = 1.5$, $r/D = 0.3$, cold; computations contain first shock-cell mode only. ——, Norum & Seiner (1982*b*); - - -, computation.

hot $M_j = 1.22$ mean flow spreading rate is substantially greater than the base flow spreading rate which qualitatively agrees with many observations of hot jet spreading rates.

Tam *et al.* (1985) showed that the jet shock-cell structure could be represented well by a sum of the zero-frequency eigenmodes of the fully-expanded mean flow. Here, following the same approach, but only including the first eigenmode, we compare computations for the two cold jet cases and the experimental pressure measurements of Norum & Seiner (1982*b*). Figure 8(*a*) shows a comparison between the first shock-cell mode and experiment. Although the agreement in phase is good, there is an over-prediction in the shock-amplitude. It is not clear at this time what the cause for this discrepancy is. Both Tam *et al.* (1985) and our computations show a similar but smaller-magnitude error for a $M_j = 1.17$, $M_d = 1.0$ jet (not shown here, see Ray 2006). Possible explanations include nonlinear effects or the effect of mean flow spreading – we have followed Tam *et al.*'s recommendation and neglected the non-parallel flow correction which is produced by the multiple-scale analysis. The agreement between computation and experiment is better for the $M_j = 1.36$ case (figure 8*b*). There is some disagreement downstream of the end of the potential core where the experimental

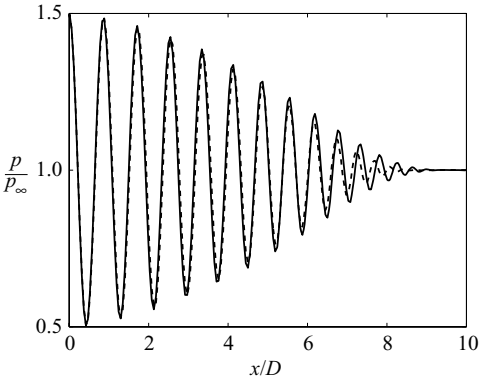

FIGURE 9. Computed shock-cell pressure at $r/D = 0$, $M_j = 1.22$, $M_d = 1.0$, first shock-cell mode with temperature ratio: ——, cold; - - -, $T_j/T_\infty = 1.7$.

shock-cells decay rapidly. This feature, which is believed to be sensitive to the presence/strength of screech, is not reproduced by the computations. Figure 9 compares the centreline pressure for the first shock-cell mode for the cold and hot $M_j = 1.22$ jets. We see that heating has little effect on the shock structure which is in qualitative agreement with experiments (Wishart 1995). While there are tangible discrepancies between computation and experiment, the goal of this investigation is not to mimic particular experiments. Rather, we simply require physically reasonable mean flows and shock-cell solutions, and we believe that the results shown here satisfy this requirement.

We have not shown the higher shock-cell modes because only the first shock-cell mode is included in our shock-noise computations. We justify this simplification in § 5.2.1.

4.3. *Instability waves*

This section presents results from linear stability computations over a range of frequencies and azimuthal wavenumbers. We focus on the streamwise evolution of the instability wave energy and phase velocity. Frequencies which are relevant to the shock-noise problem ($0.5 \leqslant St \leqslant 1.0$) are investigated, but we do not ignore lower frequencies. These modes tend to show the largest growth and are related to the generation of low-frequency mixing noise.

The integrated disturbance kinetic energy is used to characterize the instability wave amplitude,

$$K(x) = \int \frac{\overline{\rho}(u_j u_j^*)}{2} r \, \mathrm{d}r. \tag{4.1}$$

We compute the phase velocity using the PSE eigenvalue: $c_{ph} = \omega/\alpha_r$. Figure 10(a) shows the instability wave energy for the cold $M_j = 1.22$ jet for frequencies, $St = 0.3, 0.6, 0.9$ and azimuthal mode numbers, $m = 0, 1, 2$. The energy for each mode is normalized to be unity at $x = 0$, so figure 10 shows the energy growth relative to the energy at the nozzle. As frequency increases, energy growth decreases and the streamwise location of peak energy moves upstream. Also, $m = 1$ is the most amplified mode for all of the frequencies and azimuthal modes; however, the highest frequency is considerably more 'three-dimensional' than the lowest. In general, as frequency increases, energy is distributed more evenly across the azimuthal modes. Higher azimuthal modes, $m > 2$, show a regular reduction in growth as mode number

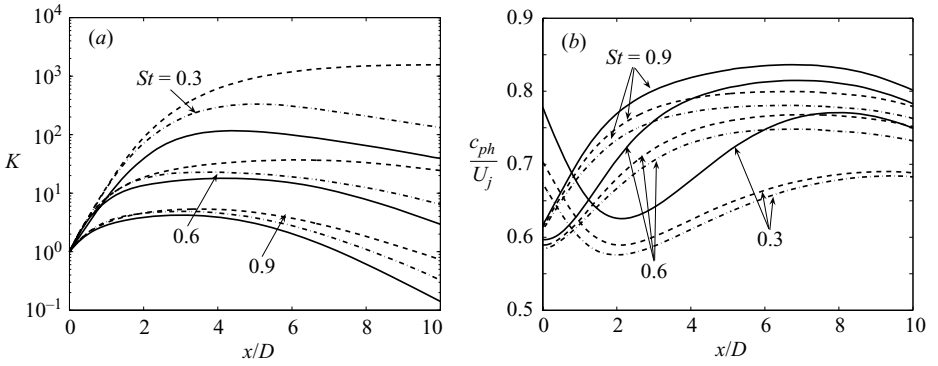

FIGURE 10. Instability wave (*a*) energy growth and (*b*) phase velocity on a $M_j = 1.22$ cold jet. ——, $m = 0$; - - - $m = 1$; —·—, $m = 2$.

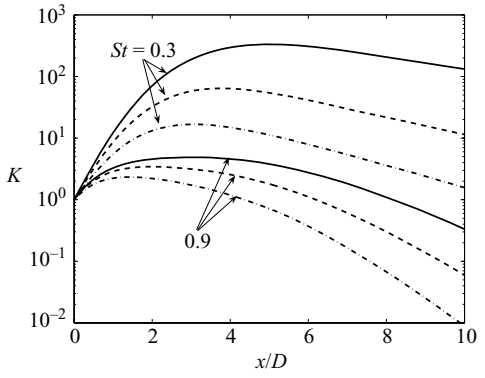

FIGURE 11. Instability wave energy growth on a $M_j = 1.22$ cold jet, higher azimuthal mode numbers. ——, $m = 2$; - - -, $m = 3$; —·—, $m = 4$.

is increased (figure 11) and we do not consider them further. The phase velocity c_{ph}/U_j is shown in figure 10(*b*) for $m = 0, 1, 2$, $St = 0.3, 0.6, 0.9$. The phase velocities for the lowest frequency, $St = 0.3$ range between ~ 0.6 and ~ 0.75 in agreement with experimental measurements of large-scale structure convection velocities. The higher frequencies for $x/D > 1$ tend to have higher phase velocities. Also, higher azimuthal mode numbers tend to have lower phase velocities. Using Tam & Tanna's 'Mach wave' reasoning, instability waves with higher phase velocities are expected to produce shock-noise which radiates at larger inlet angles.

The $M_j = 1.36$ cold jet instability waves are similar to the $M_j = 1.22$ case as can be seen by comparing figures 10 and 12. Figure 13 displays the energy and phase velocities for the hot $M_j = 1.22$ jet instability waves. Most of the basic trends remain the same as in the previous two cases though there are some notable differences. The energy of the hot jet instabilities grows downstream of the end of the potential core ($x > 5$) whereas the cold cases show regular decay. This growth is due to strong Mach waves which, when radiating at shallow angles, can contribute significantly to the integrated energy (equation (4.1)) at downstream locations where the instability waves are decaying in the jet shear layer. Since our primary interest is instability amplitude within the jet, it is desirable to remove the influence of the Mach waves; however, there does not seem to be a rigorous method for accomplishing this.

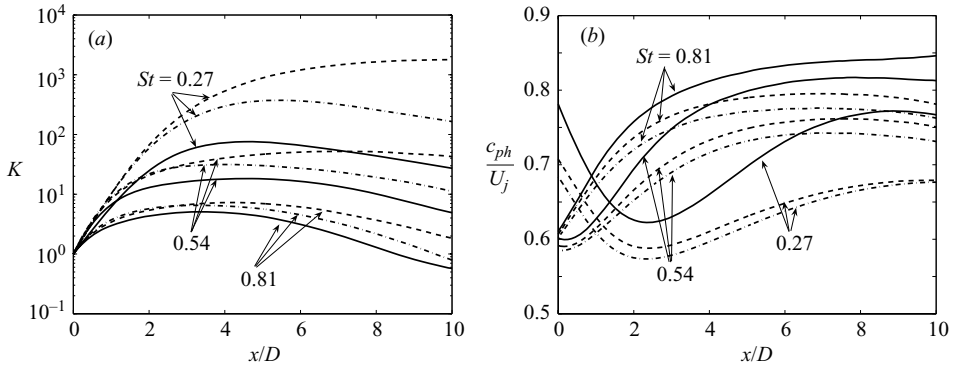

FIGURE 12. Instability wave (*a*) energy growth and (*b*) phase velocity on a $M_j = 1.36$ cold jet. ——, $m = 0$; - - -, $m = 1$; $-\cdot-$ $m = 2$.

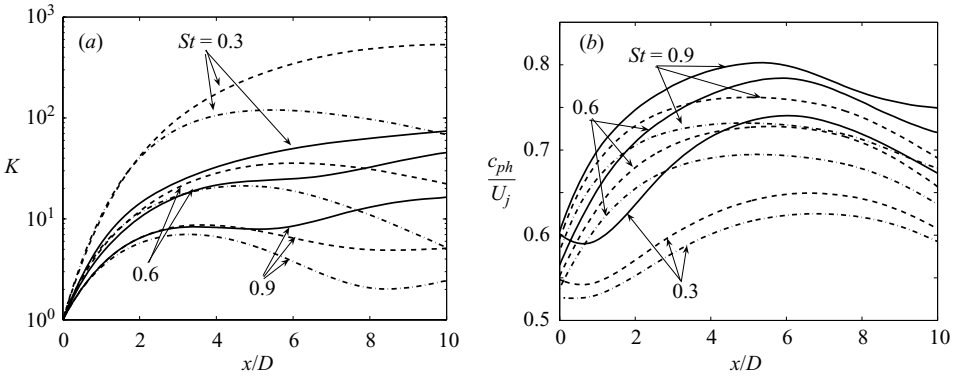

FIGURE 13. Hot jet instability wave (*a*) energy growth and (*b*) phase velocity, $M_j = 1.22$. ——, $m = 0$; - - -, $m = 1$; $-\cdot-$ $m = 2$.

We use two simple modifications to the definition of the integrated kinetic energy (equation (4.1)), the energy norm used in the PSE numerical method (equation (3.12)) was not modified): (i) the r-weighting from the energy integral is removed and (ii) the upper limit of integration is reduced to $r/D = 2.0$; with these changes, the 'modified disturbance kinetic energy', K^* for the hot jet is shown in figure 14(*a*). We see that the basic behaviour is now in agreement with the cold computations. Figure 14(*b*) compares the cold and hot instability wave energies for $m = 0, 1$ and $St = 0.3, 0.9$. A trend can be seen – at the lower frequency, the cold jet instabilities are considerably more energetic whereas at the higher frequency, the energies are similar. To gain a fuller view of the effect of jet temperature, we have also computed $St = 0.6$ instability waves with $T_j/T_\infty = 2.7$. The modified kinetic energies and phase velocities are shown in figure 15. For $m = 1$ and $m = 2$ (not shown), as the temperature ratio is increased, peak energy increases, while the axisymmetric mode shows an initial decrease in energy followed by an increase. Such 'irregular' behaviour at intermediate frequencies can be anticipated from figure 14. The phase velocity (relative to the jet velocity) decreases as temperature increases downstream of $x \sim 2$. However, caution should be used in applying this result, given the artificial nature of the energy measure used. Further study on the effect of heating on the instability waves is required.

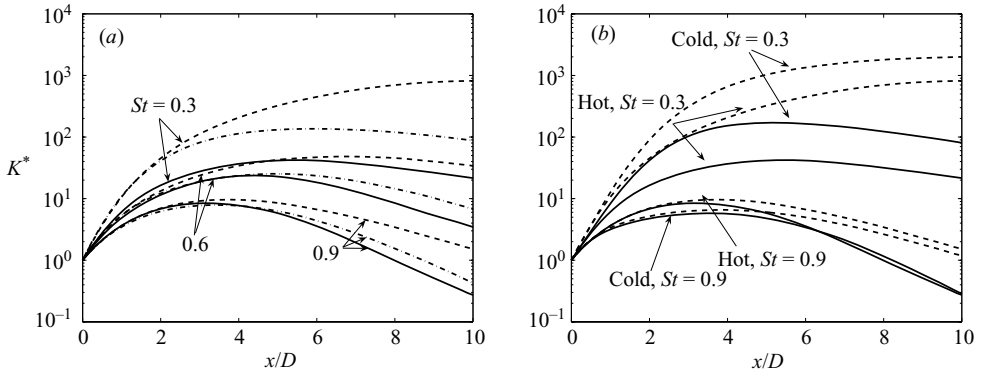

FIGURE 14. Modified instability wave kinetic energy for (*a*) hot $M_j = 1.22$ jet and (*b*) hot and cold $M_j = 1.22$ jets. ——, $m = 0$; - - -, $m = 1$; - - - $m = 2$.

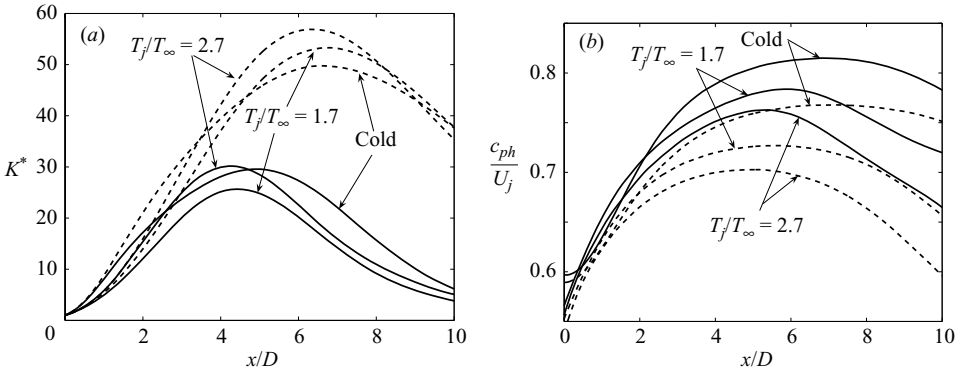

FIGURE 15. Effect of jet temperature on $St = 0.6$ instability wave, $M_j = 1.22$; (*a*) energy growth and (*b*) phase velocity; ——, $m = 0$; - - -, $m = 1$.

To a large extent, the radial structure of instability waves is dictated by the symmetry conditions and near-centreline behaviour of a given azimuthal mode, m. Only the first two azimuthal modes possess disturbances which are non-zero at the centreline. The streamwise velocity and thermodynamic variables can be finite at $r = 0$ for $m = 0$ while the radial and azimuthal velocities may be non-zero for $m = 1$. All other quantities must go to zero at the centreline. Thus, for $m > 1$, we expect instability waves to be confined in the jet shear layer, whereas penetration of the disturbances into the jet core is possible for $m = 0, 1$. This behaviour can be illustrated by introducing and examining the quantity, $r_\infty(x)$, which we define as the radial position at which the disturbance kinetic energy is maximum. Figure 16 plots r_∞ for the cold and hot $M_j = 1.22$ cases. The $m = 1$ and $m = 2$ curves generally stay confined to the shear layer, gradually moving inward as the shear layer spreads. The axisymmetric mode displays considerably more complicated behaviour. The $m = 0$ maximum 'jumps' from the centre of the shear layer to the inner edge of the shear layer which it then follows to the end of the potential core. A more complete view of this behaviour is presented in figure 17 which shows radial profiles of u_x, u_r and ρ, at three streamwise locations, $x = 0.5, 2, 6$, and three azimuthal mode numbers, $m = 0, 1, 2$. Only two of the nine plots show significant penetration into the jet core: (*a*) $u_x, m = 0$ and (*e*) $u_r, m = 1$

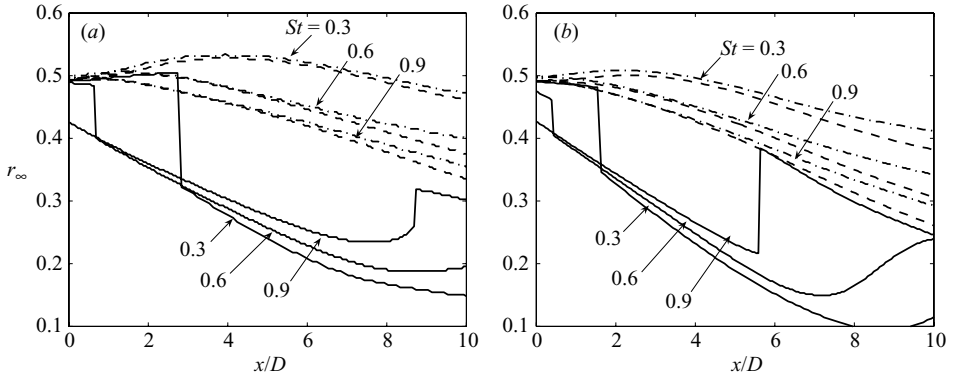

FIGURE 16. Radial location of maximum instability wave kinetic energy for (*a*) cold and (*b*) hot, $M_j = 1.22$ jets. ——, $m = 0$; - - -, $m = 1$; —·—, $m = 2$.

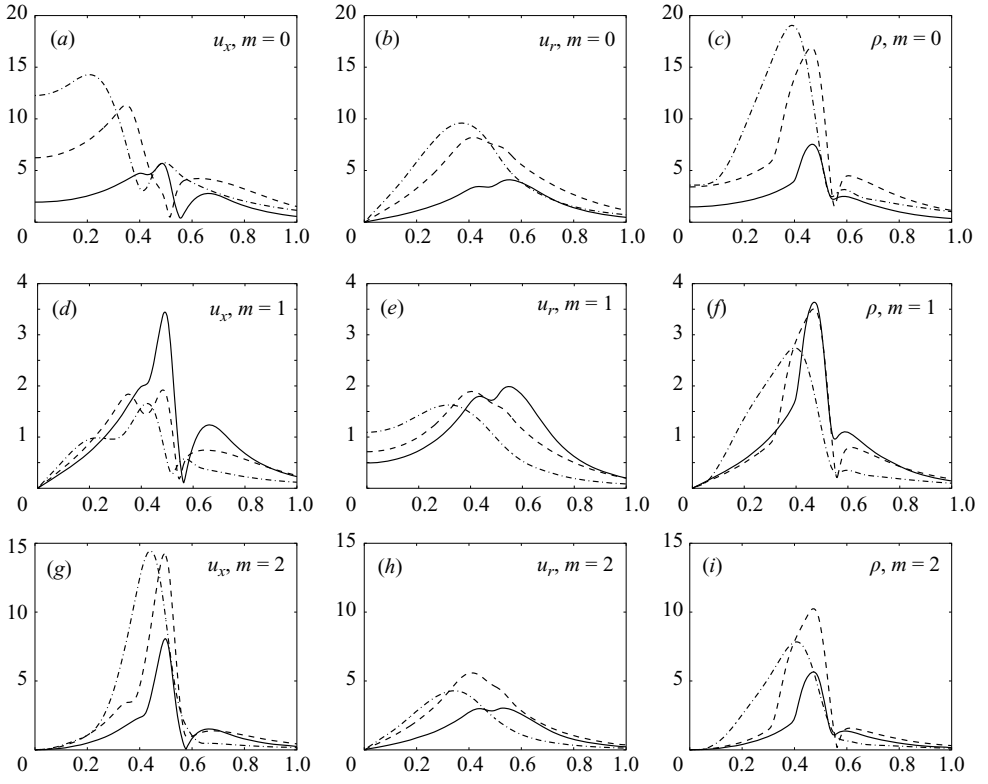

FIGURE 17. Instability wave radial profiles, $|f|$ *vs.* r; $M_j = 1.22$ cold jet, $St = 0.6$; the quantity plotted and azimuthal mode number, m, are labelled on the individual plots. ——, $x = 0.5$; - - -, $x = 2.0$; —·—, $x = 6.0$.

which is in agreement with the discussion of near-centreline behaviour of Fourier modes above.

Clearly, instability waves which peak closer to the jet centreline will interact more vigorously with the jet shock-cell structure. Thus, even though the helical ($m = 1$)

instability waves tend to have larger growth rates than the axisymmetric modes, the axisymmetric modes may generate more shock-noise.

5. Shock-noise

Earlier sections discussed computations of jet mean flows, shock-cell structure and instability waves. Now, these elements are used together to compute the sound generated by the (weak) interaction between linear instability waves and the shock-cell structure in three supersonic jets.

Our analysis will focus on two aspects of the sound fields: (i) directivity and (ii) amplitude. In examining the directivity, we attempt to isolate the factors which determine the peak radiation angles. The analysis of the sound amplitudes will investigate what features of the sources are most significant in determining the relative peak sound amplitudes. Properties of the mean flows, instability waves, and shock-cell structures are connected to the trends observed in the sound fields.

5.1. *The acoustic field of the $M_j = 1.22$ cold jet*

We begin with an examination of the sound fields for the $M_j = 1.22$, $M_d = 1.0$ cold jet. Figure 18(*a*) is a composite plot which shows instantaneous pressure contours for the axisymmetric ($m = 0$) mode along with contours of mean streamwise velocity and shock-cell pressure. Sound radiating away from the jet in the upstream direction can be clearly observed. The source consists of contributions from three instability waves at frequencies $St = 0.6, 0.75, 0.9$, and a clearer picture of the sound field is obtained by extracting the Fourier components of the pressure field at these three forcing frequencies. These fields are shown in figure 18(*b–d*), and they illustrate a well-known feature of shock-noise: as inlet angle increases, the peak sound frequency also increases. Another view of the radiated sound is obtained by extrapolating the near-field pressure to the far field. Figure 19(*a*) shows the far-field pressure for the base case, $m = 0$. Sound at higher frequencies is radiated at larger inlet angles with smaller amplitudes. Identical trends are observed for $m = 1$ and $m = 2$ (figure 19*b, c*). Also shown in the figures as symbols are Rayleigh equation (parallel mean flow) solutions which neglect the effect of mean flow spreading on the sound propagation (the mean flow at $x = x^*$ is used, where x^* is defined in § 5.5). For most of the cases, the Rayleigh solutions provide a good estimate of the full solution. This comparison is useful for several reasons. First, the Rayleigh equation can be solved much faster than the LEE, so for cases with good agreement, the Rayleigh equation can be solved easily with different combinations of the various source terms to gain insight into sound generation mechanisms. Alternatively, the presence of substantial differences between the two solution methods is indicative of significant refraction effects owing to the spreading of the mean flow. It is well known that the effect of mean flow spreading has the greatest impact on sound radiated at shallow angles. This effect is reflected in the increased discrepancies between the LEE and Rayleigh solutions at small inlet angles.

5.2. *Source filtering and 'radiating sources'*

We now shift our focus from the sound fields to the shock-noise sources. Consider a streamwise Fourier decomposition of the shock-noise source terms. Not all components radiate sound, and it is useful to isolate those that do (as in Freund 2001). Formally, a Fourier transform is applied to the sources ($x \rightarrow k$) at a given frequency,

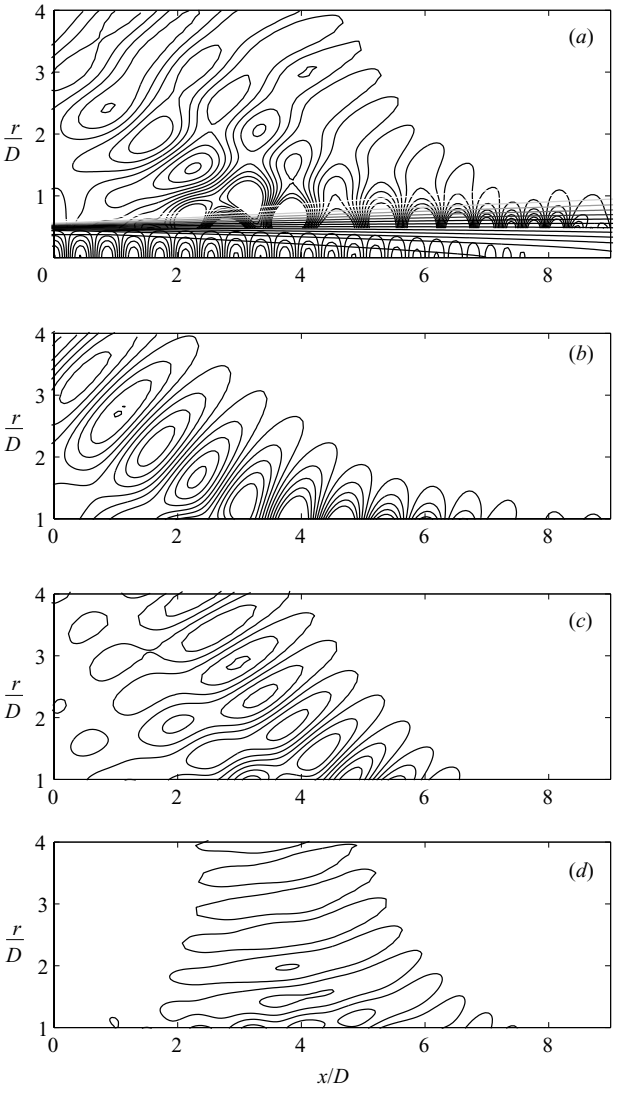

FIGURE 18. Results for the $M_j = 1.22$ cold jet, $m = 0$; (*a*) composite plot showing (i) shock-cell pressure in interior of jet, (ii) contours of streamwise mean velocity in jet shear layer, and (iii) shock-noise (instantaneous pressure) outside of jet; $M_j = 1.22$, $St = 0.6$, 0.75, 0.9, $m = 0$; (*b*) real part of Fourier-transformed pressure, $St = 0.6$; (*c*) real part of Fourier-transformed pressure, $St = 0.75$; (*d*) real part of Fourier-transformed pressure, $St = 0.9$.

ω. For a parallel mean flow, only those components which satisfy the condition

$$\left|\frac{\omega}{k}\right| > a_\infty, \tag{5.1}$$

radiate sound. Then, if we filter out the non-radiating components and apply an inverse Fourier transform, we obtain the 'radiating sources'. The radiation condition (equation (5.1)) is not strictly valid for spreading mean flows. For the cases of interest in this study, the mean flows can be considered slowly spreading, and (5.1) should be a good approximation. Nevertheless, we do not use the sharp cutoff filter implied by (5.1); instead, we use a smooth filter function with a 'safety factor', Δ, included to

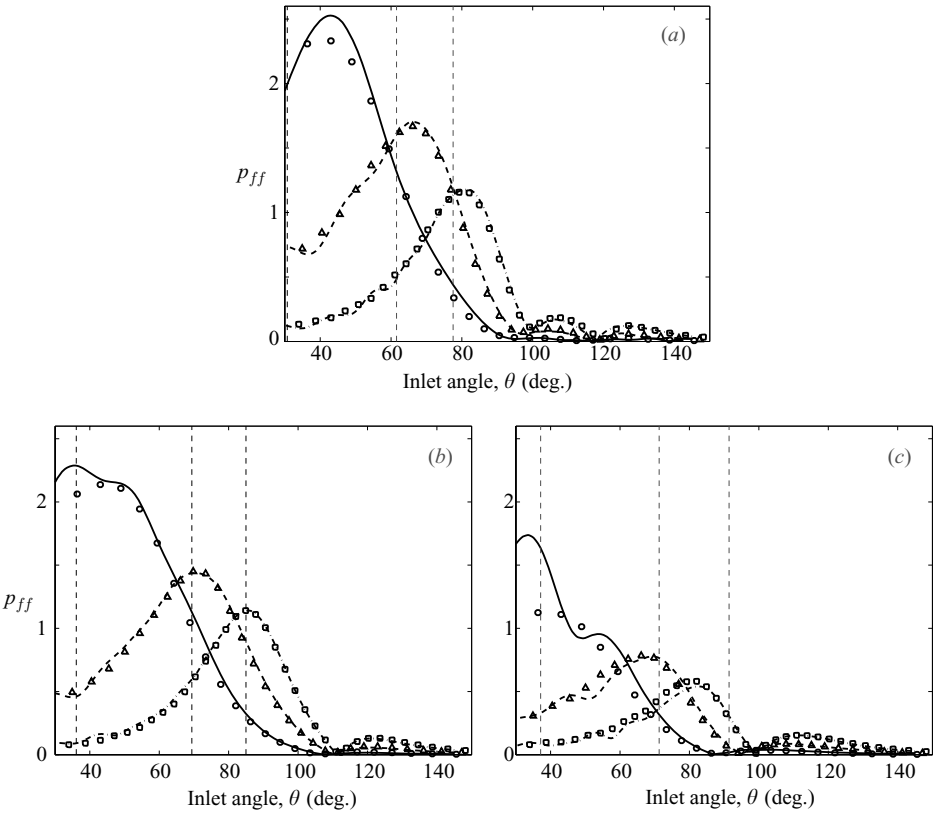

FIGURE 19. Far-field pressure, $M_j = 1.22$, (*a*) $m = 0$, (*b*) $m = 1$, (*c*) $m = 2$. ——, $St = 0.6$ (LEE); - - -, $St = 0.75$ (LEE); $-\cdot-$, $St = 0.9$ (LEE); Symbols indicate Rayleigh equation solutions and vertical lines indicate effective Mach angles which are discussed in § 5.4.

account for the approximate nature of (5.1),

$$f_{filt} = 0.5\left\{1 + \tanh\left[3\left(\frac{k}{\omega} - 1 - \Delta^-\right)\right]\right\}\left\{1 - \tanh\left[3\left(\frac{k}{\omega} + 1 + \Delta^+\right)\right]\right\}, \qquad (5.2)$$

and we use $\Delta^- = 1$ for cold cases, $\Delta^- = 0$ for hot cases and $\Delta^+ = 1$ for all cases.

Let us take the axisymmetric $St = 0.75$ mode for the cold $M_j = 1.22$ jet as an illustrative example. Figure 20 shows the streamwise Fourier transform of the mass source at $r = 0$, $\hat{S}_\rho(k, r = 0)$, plotted against k/ω. Now, the radiating components are contained within $-1 \lesssim k/\omega \lesssim 1$ as indicated in the figure. Two peaks can be readily identified. One of these is non-radiating and downstream-propagating whereas the other produces shock-noise at upstream-directed angles. Note that the amplitude of the non-radiating peak is larger than the amplitude of the shock-noise peak – this indicates that the unfiltered source may give a misleading view of sound-generation. An alternate perspective is gained by filtering out the non-radiating components as shown in the figure and computing the inverse transform of the filtered spectrum. Figure 21 shows contours of the unfiltered (figure 21*a*) and filtered (figure 21*b*) mass source. There is a substantial qualitative difference between the two sources. Filtering removes small-wavelength components and we are left with two 'source regions': the initial shear layer and the core of the jet near the end of the potential core. Before proceeding further, we should verify that the two sources produce the same sound

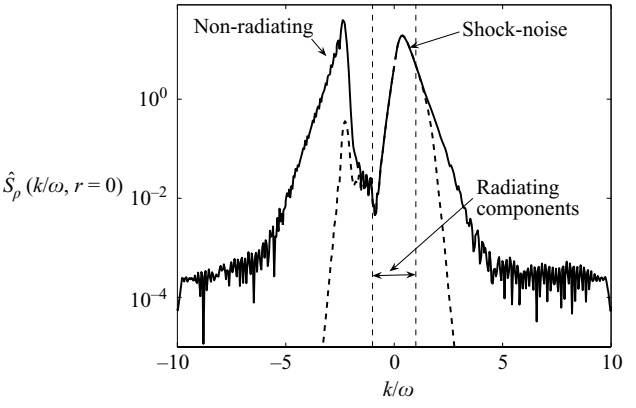

FIGURE 20. Source spectra for mass source along centreline, $M_j = 1.22$, cold jet, $m = 0$, $St = 0.75$. ——, unfiltered; - - -, filtered.

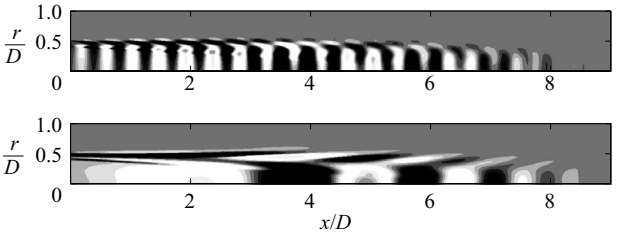

FIGURE 21. Effect of filtering on shock-noise sources. Contours of real part of mass-source for the $M_j = 1.22$ cold jet, $St = 0.75$, $m = 0$ are shown; (*a*) unfiltered; (*b*) filtered.

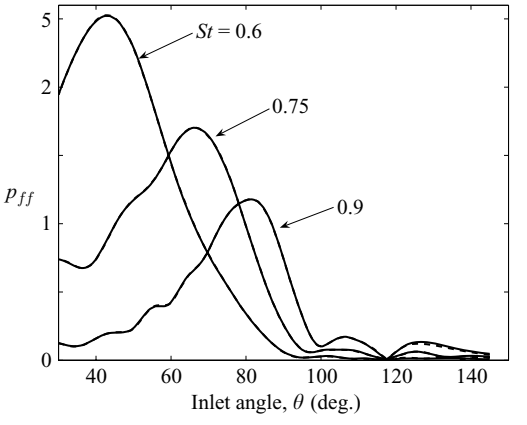

FIGURE 22. Far-field pressure computed with filtered sources, $M_j = 1.22$, $m = 0$. $St = 0.6$, 0.75, 0.9; Solutions with unfiltered sources (- - -) are also plotted, but they are nearly indistinguishable from the filtered-source results.

fields. Figure 22 compares sound fields obtained by solving the LEE with filtered and unfiltered sources for the $M_j = 1.22$ cold jet with $St = 0.6,\ 0.75,\ 0.9$ and $m = 0$. For all practical purposes, the sound fields are the same. Returning to the filtered source 'field' shown in figure 21, we note that the relative importance of the two source regions is frequency-dependent. At higher frequencies, the shear-layer component increases in

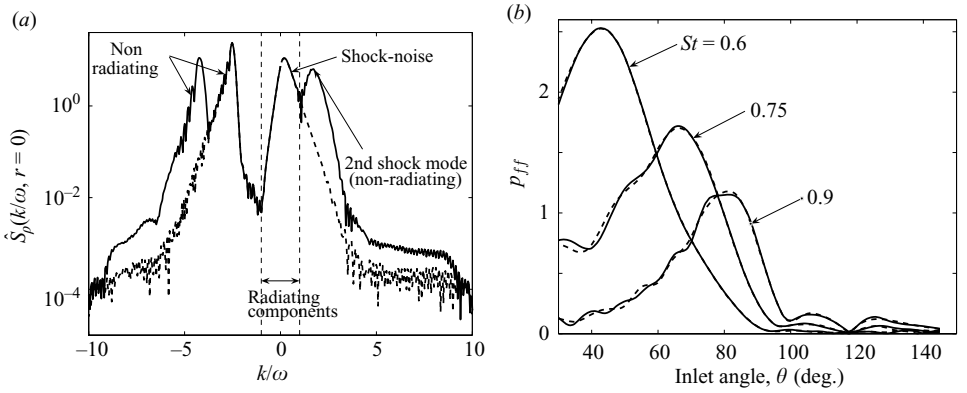

FIGURE 23. Effect of second shock mode on source spectra and far-field sound for $M_j = 1.22$ cold jet, $m = 0$; (*a*) Source spectra for mass source along centreline, ——, first and second shock-cell modes; - - -, first shock-cell mode only; (*b*) far-field pressure, ——, first and second shock-cell modes; - - -, first shock-cell mode only.

significance whereas at lower frequencies the jet core component dominates. This jet core component only appears for axisymmetric modes; sources for non-axisymmetric modes contain only shear-layer components (see figures 25, 32).

5.2.1. *Higher shock-cell modes*

If the pressure mismatch of a supersonic jet is small, the jet shock-cell structure can be modelled as the sum of zero-frequency linear eigenmodes of the mean flow. For the cases considered in this study, only the first shock-cell mode radiates significant levels of sound to the far field. Typically, we have checked this statement by computing the local Mach angle (introduced below, equation (5.5)). We can also examine the influence of the higher shock-cell modes on the source spectrum. Figure 23(*a*) shows mass-source spectra for the $M_j = 1.22$ cold jet with $m = 0$, $St = 0.9$. Spectra for two cases are shown – a source including the first shock-cell mode only and a source including the first two shock-cell modes. We see that when the second shock-cell mode is included, two new peaks appear in the spectrum. The wavenumbers of these peaks, however, lie outside of the range of radiating wavenumbers. Figure 23(*b*) compares the far-field sound radiated by the first two shock modes with that radiated by the first mode alone. There are minor differences between the two curves, but practically, the effect of the second shock-cell mode on the sound is negligible. At higher frequencies, the higher shock-cell modes will increase in significance. However, since a linear instability wave representation of turbulence becomes increasingly suspect at higher frequencies, we have not considered such cases here.

5.2.2. *Coarse-grid computation*

Note that large-amplitude small-wavelength disturbances will be generated by the higher shock-cell modes placing additional strain on the numerical method. There are two approaches which can remove this strain. The first is to ignore the higher modes altogether; the second is to construct the full source and filter non-radiating components. A more general methodology related to the second approach requires the resolution of only the large-wavelength radiating components. Then, (relatively) coarse grids could be used resulting in significant savings in computation time. The procedure is as follows: compute the source spectra, filter out non-radiating components, spectrally interpolate onto a coarser grid, and finally solve the LEE with the

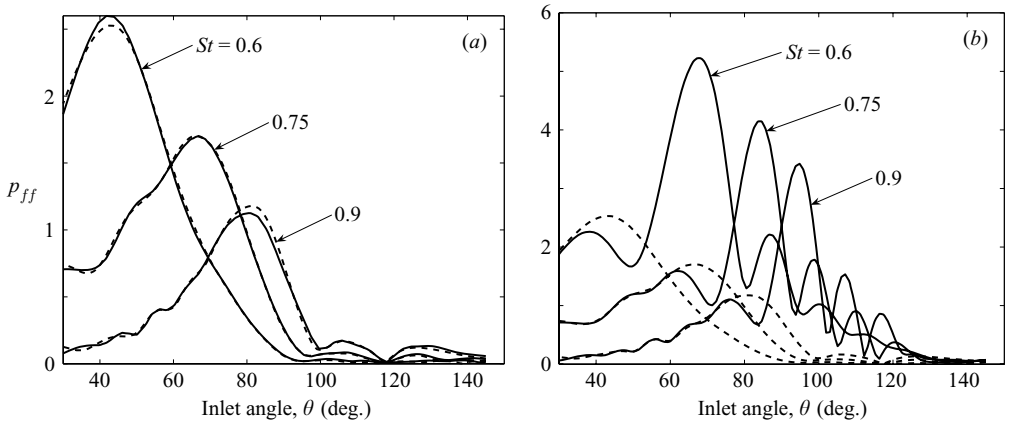

FIGURE 24. Far-field pressure from coarse-grid computations, $M_j = 1.22, m = 0$. (*a*) ——, coarse grid ($Nx = 65$) solutions with source filtering; - - -, full ($Nx = 512$) solutions with unfiltered sources. (*b*) Coarse-grid results with unfiltered sources: ——, $Nx = 65$; - - -, $Nx = 129$.

filtered sources on a coarse grid. We have carried out a few coarse-grid computations for the $M_j = 1.22$ cold, $m = 0$ case. Figure 24(*a*) compares the sound fields produced by a 'full' computation which use 513 grid points in the streamwise direction and a coarse computation which uses 65 grid points. There is a slight difference between the solutions at the peaks, but overall, the agreement is very good. Figure 24(*b*) compares coarse-grid solutions without source-filtering. For $Nx = 129$, the absence of source filtering has little effect, but we see a dramatic degradation of the solution with $Nx = 65$, and source-filtering is clearly required in order to produce an accurate solution. It is clear that poorly resolved non-radiating components of the source can corrupt the far-field sound.

5.2.3. *Localized vs. distributed sources*

Harper-Bourne & Fisher (1973) modelled shock-noise sources as an array of point sources, whereas the measurements of Norum & Seiner (1982*a*) indicate that shock-noise sources are spatially distributed. In this section, we argue that, for the cases considered in this study, these viewpoints are not mutually exclusive; each may be appropriate depending on the perspective that is adopted. The localized-source model is reasonable if we consider the full source due to several shock-cell modes. If only one shock-cell mode is considered, the sources are less localized; if only the radiating components are used, the sources are decidedly distributed in space. This is illustrated in figure 25 for the $St = 0.6$, $m = 1$, r-momentum source for the $M_j = 1.22$ cold case. The first three shock-cell modes have been included in the construction of these sources. Figure 25(*a*) shows the 'full' source, and we can see localized sources centred at points where the shock-cells interact with the jet shear layer. As one moves downstream, the higher shock-cell modes decay away, and the sources become somewhat more distributed. Figure 25(*b*) is the filtered source – again, filtering has a dramatic effect on the source structure. It is likely that the rate of decay of higher shock-cell modes is connected to the strength/presence of screech tones. For cases where screech is suppressed, the higher-modes are expected to persist farther downstream, and the Harper-Bourne & Fisher (1973) source representation should improve.

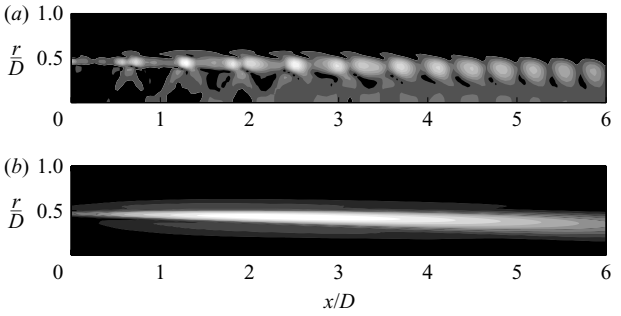

FIGURE 25. Localized *vs.* distributed sources, contours of r-momentum source magnitude for the $M_j = 1.22$ cold jet, $St = 0.6$, $m = 1$. Three shock-cell modes are included in the source. (*a*) Unfiltered; (*b*) filtered.

5.3. *Sound budget*

The computed shock-noise is the superposition of sound radiated by each of the sources in the governing equations. It is useful to decompose the sound into these individual components. However, solving the full LEE for each component is a computationally intensive task. As an alternative, simpler approach, we solve the Rayleigh equation and obtain the sound radiated by sources in each of the primitive variable equations.

As noted in Appendix B, the linearized Euler equations with a parallel base flow and time harmonic, spatially compact sources can be written as an inhomogeneous Rayleigh equation,

$$\mathscr{R}\{\tilde{p}\} = -\mathrm{i}\omega(1+\overline{U}_x\kappa)\left(\frac{\tilde{S}_\rho}{\overline{\rho}} + \frac{\overline{\rho}\tilde{S}_s}{(\gamma-1)}\right) + \mathrm{i}\omega\kappa\tilde{S}_{u_x} + \frac{1}{r}\frac{\mathrm{d}(r\tilde{S}_{u_r})}{\mathrm{d}r} - \frac{2\kappa}{1+\overline{U}_x\kappa}\frac{\mathrm{d}\overline{U}_x}{\mathrm{d}r}\tilde{S}_{u_r} + \frac{\mathrm{i}m}{r}\tilde{S}_{u_\theta}, \tag{5.3}$$

where $\mathscr{R}$ represents the compressible Rayleigh equation operator. This equation shows that sound at a given frequency and azimuthal mode number, $\tilde{p}$, is produced by the weighted sum of a mass source ($\tilde{S}_\rho$), entropy source ($\tilde{S}_s$), and three momentum sources ($\tilde{S}_{u_x}, \tilde{S}_{u_r}, \tilde{S}_{u_\theta}$). The individual sound fields corresponding to these five sources make up what we refer to as the 'sound budget'. For example, the sound due to the mass source is the solution to:

$$\mathscr{R}\{\tilde{p}\} = -\mathrm{i}\omega(1+\overline{U}_x\kappa)\left(\frac{\tilde{S}_\rho}{\overline{\rho}}\right).$$

This budget is shown for the $m = 1$, $St = 0.75$ case in figure 26. The r-momentum source is most significant though there are tangible contributions from the other sources as well. Comparing the 'r-momentum' sound amplitude to the overall amplitude (figure 27*b*), we see that there is good agreement in peak radiation angle at all three frequencies, but at $St = 0.6$, there is a large difference in amplitude. Also, at $St = 0.9$, the total sound is less than the r-momentum sound. This indicates that there must be destructive interference between the different sound components. The mass source is the dominant source for the $m = 0$ and $m = 2$ modes (figures 27*a* and 28*a*), however, the peak radiation angles do not match as well as they do for $m = 1$, particularly at $m = 2$. Figure 28(*b*) shows the real part of the sound budget for $m = 2$, $St = 0.9$. Though the sound due to the mass source is 'loudest', there is substantial

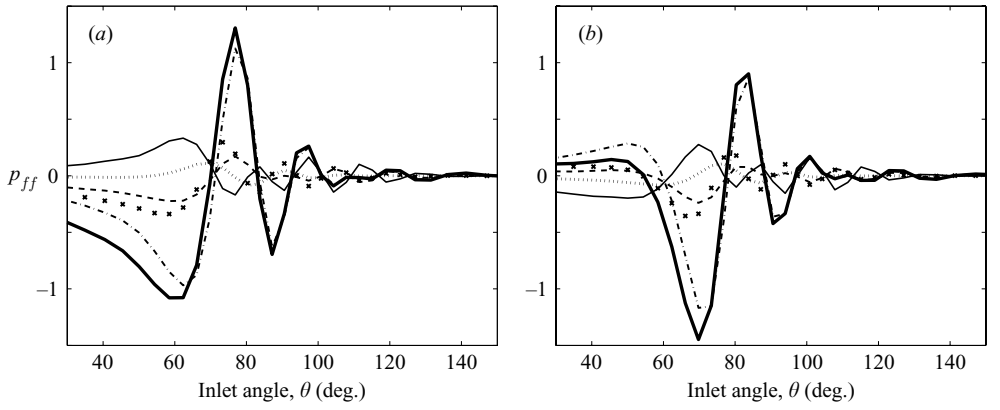

FIGURE 26. Sound budget, $M_j = 1.22$, $m = 1$, $St = 0.75$, (*a*) real and (*b*) imaginary components of far-field pressure generated by: ——(thick), full source; ——, mass source; ——, x-momentum source; —·—, r-momentum source; ···, θ-momentum source; ×, entropy source.

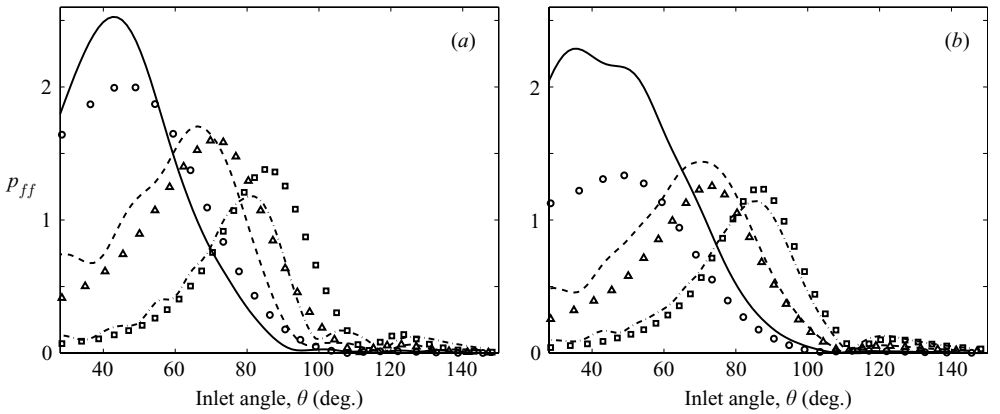

FIGURE 27. Far-field pressure for $M_j = 1.22$ cold jet, (*a*) $m = 0$ sound due to full source (lines) and mass source (symbols), and (*b*) $m = 1$ sound due to full source (lines) and r-momentum source (symbols); —— and ○, $St = 0.6$; - - - and △, $St = 0.75$; —·— and □, $St = 0.9$.

interference from the other sources modifying the amplitude and directivity. Thus, the individual azimuthal modes possess fairly distinct sound generation/radiation mechanisms. The dominance of the mass and r-momentum sources identified here will be used later in analysing general trends in the shock-noise data.

5.4. *Effective Mach angle*

The observed trends in the peak radiation angles can be explained with Tam & Tanna's (1982) 'Mach wave' model. We first define a 'local source phase velocity',

$$c_s(x) = \frac{\omega}{k_t - k_s}, \tag{5.4}$$

where ω is the instability wave frequency, k_s is the local shock-cell wavenumber, and k_t is the local instability wave wavenumber. A 'local Mach angle' readily follows,

$$\theta_M(x) = \cos^{-1}(1/c_s). \tag{5.5}$$

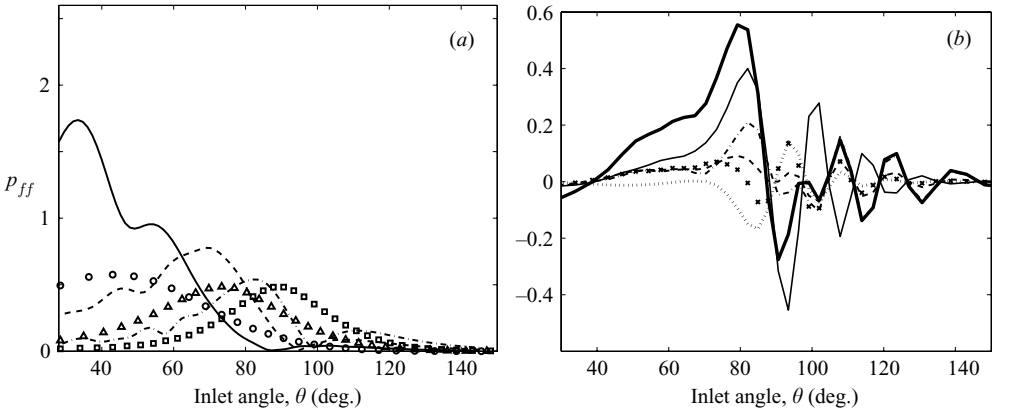

FIGURE 28. Far-field pressure for $M_j = 1.22$ cold jet $m = 2$, (a) sound due to full source (lines) and mass source (symbols): —— and ○, $St = 0.6$; - - - and △, $St = 0.75$; —·— and □, $St = 0.9$, and (b) real part of sound generated by: ——, full source; ——, mass source; - - -, x-momentum source; —·—, r-momentum source; ···, θ-momentum source; ×, entropy source.

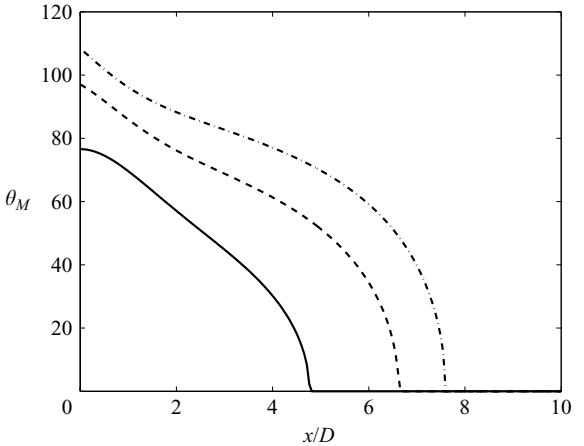

FIGURE 29. Local Mach angle, $M_j = 1.22, m = 0$. —— $St = 0.6$; - - -, $St = 0.75$; —·—, $St = 0.9$.

The local Mach angle is plotted in figure 29 for the axisymmetric mode. A finite range of 'potential' strong radiation angles exists for each frequency. As frequency increases, the width of this range increases. This increase in width has little effect on the actual sound fields since the linear instability waves also decay more quickly at higher frequencies. However, in realistic turbulent flows, nonlinear effects which are neglected here could allow these higher-frequency instabilities to persist farther downstream. Then, we would expect stronger higher-frequency radiation at shallower angles as indicated by figure 29. We define an 'effective' Mach angle, $\theta_M(x^*)$ by determining the streamwise locations from which the strongest sound radiates, x^*. We use the results from the sound budget analysis to define x^* as the streamwise location where the radially integrated filtered mass source is maximum for $m = 0, 2$; the r-momentum source is used for $m = 1$. Applying this approach to the $M_j = 1.22$ cold jet gives the results indicated by vertical dashed lines in figure 19. The agreement is very good for almost all cases. An exception is $m = 2$, $St = 0.9$ which is not surprising since figure 28 shows that the peak radiation angles of sound generated by the mass source alone do

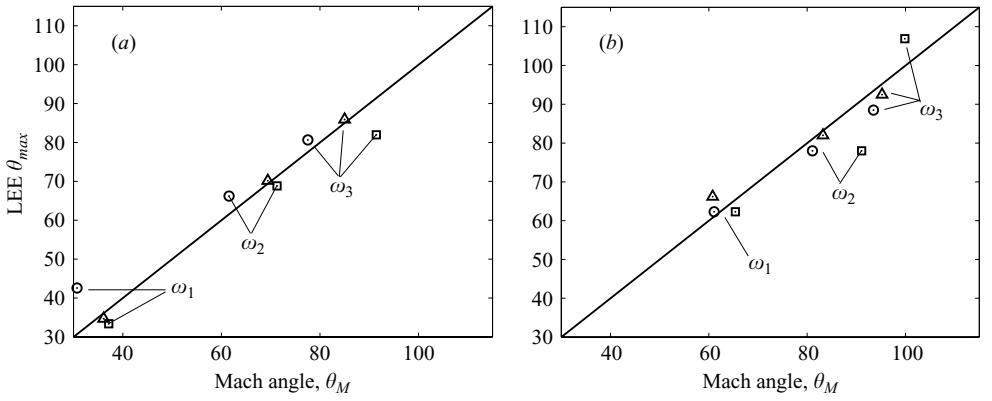

FIGURE 30. Comparison of LEE-computed peak radiation angles (θ_{max}) and Mach angles, (*a*) $M_j = 1.22$ and (*b*) $M_j = 1.36$. ○, $m = 0$; △, $m = 1$, □, $m = 2$; $\omega_1 = 4.04$, $\omega_2 = 5.05$, $\omega_3 = 6.06$.

M_j	m	x^*	$c_{ph}(x^*)/U_j$	$2\pi/k_s(x^*)$	$\theta_M(x^*)$
1.22	0	3.97, 3.97, 3.92	0.79, 0.81, 0.82	0.76, 0.76, 0.76	30.7, 61.6, 77.5
1.22	1	4.08, 3.34, 2.97	0.75, 0.76, 0.78	0.76, 0.79, 0.80	36.1, 69.4, 85.0
1.22	2	4.23, 3.39, 2.13	0.73, 0.74, 0.73	0.75, 0.79, 0.83	37.1, 71.3, 91.4
1.36	0	4.66, 4.13, 3.6	0.79, 0.80, 0.80	1.01, 1.04, 1.06	61.1, 81.1, 93.5
1.36	1	5.40, 4.39, 3.87	0.75, 0.76, 0.77	0.97, 1.02, 1.06	60.8, 83.2, 95.2
1.36	2	4.92, 2.81, 2.81	0.73, 0.72, 0.74	1.00, 1.09, 1.09	65.4, 91.1, 99.9

TABLE 2. Effective Mach angle parameters for the cold jets. The three numbers in each table entry correspond to the frequencies ($\omega_1, \omega_2, \omega_3$) specified in the caption for figure 30; $c_{ph} = \omega/k_t$.

not match the peak radiation angles of the overall sound for this case. Comparison of 'predicted' Mach angles with the computations for the two cold cases are collected in figure 30. The agreement is very good for almost all cases except $m = 2$ at higher frequencies.

The parameters used to determine the effective Mach angles are given in table 2. Interpreting x^* as the streamwise location at which the dominant sound is generated, two trends are evident. As frequency increases, the location of sound generation tends to move upstream – higher-frequency instability waves tend to peak closer to the nozzle. The second trend is that values for x^* are larger for the higher-Mach-number case. At higher Mach number, the potential core length increases, and instability waves peak farther downstream while the shock-cell structure decays at a slower rate. The other parameters in table 2 will be discussed later when we compare Tam's (1987) model with our computations.

5.5. *Peak sound amplitudes*

The reduction in sound amplitude as frequency increases, correlates well with the corresponding decrease in instability wave growth for most of the cases (figure 31). Such a correlation does not exist when comparing the amplitudes across different azimuthal modes. For example, the instability wave energies for the $M_j = 1.36, m = 2$ case are comparable to, or greater than, the $M_j = 1.36, m = 0$ instability wave energies; however, the $m = 0$ sound amplitudes are larger. A similar trend is observed when comparing the $M_j = 1.22, m = 0$ and $m = 1$ cases. This behaviour can be understood

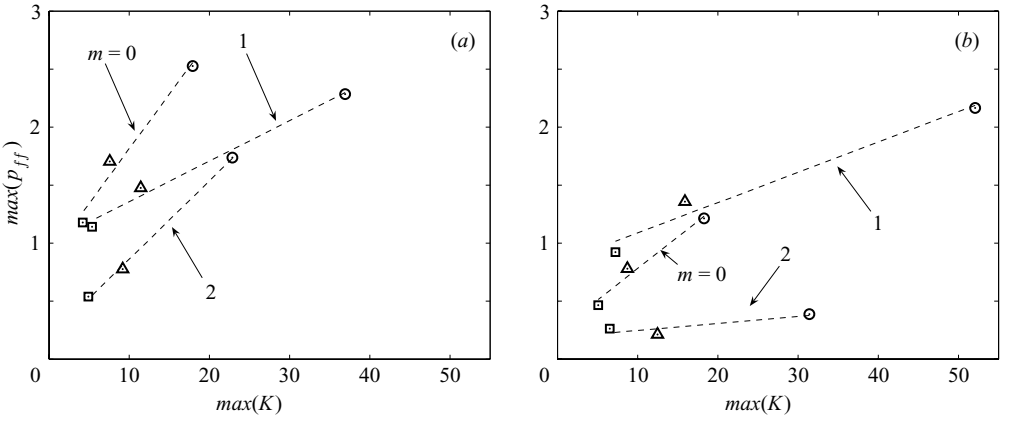

FIGURE 31. Comparison of peak sound amplitudes and peak instability wave kinetic energies for the (*a*) $M_j = 1.22$ and (*b*) $M_j = 1.36$ cold jets; ○, $\omega = 4.04$; △, $\omega = 5.05$; □, $\omega = 6.06$.

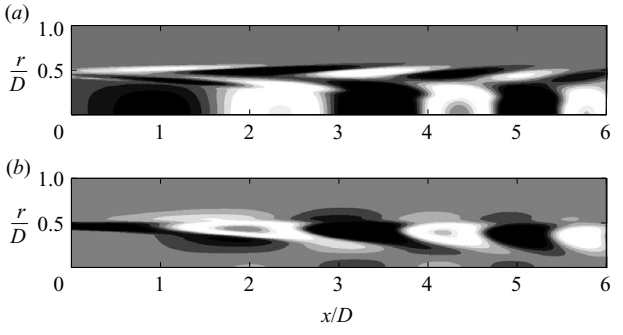

FIGURE 32. Contours of the real part of the dominant (filtered) source for the $M_j = 1.22$ cold jet, $St = 0.6$. (*a*) $m = 0$, mass source (max = 12.0); (*b*) $m = 1$, r-momentum source (max = 6.2). Each source has been normalized by its maximum amplitude which is given above.

by examining the radial structure of the instability wave. As discussed earlier, the axisymmetric instability waves tend to penetrate the jet core whereas higher modes tend to stay localized in the shear layer. Figure 32 shows the mass and r-momentum shock-noise source amplitudes for the $m = 0$, $St = 0.6$ and $m = 1$, $St = 0.6$ cases, respectively. The source amplitude and source volume for $m = 0$ is tangibly larger despite the larger growth rate of the $m = 1$ instability wave.

There is little correlation between the sound and instability wave amplitudes for the $m = 2$, $M_j = 1.36$ case. For this case, there is significant interference between the sources. In fact, the sound radiated by the r-momentum source is dominant for this case due, in part, to the cancellation of mass-source sound by the other sources. Thus, the details of the source structure are important. In the next section, we will see that source interference is also closely tied to the effect of heating on shock-noise.

5.6. *On the effect of heating on shock-noise*

The hot $M_j = 1.22$ jet shows trends which are similar to the unheated case (figure 33). A notable difference is the elevated sound levels for the hot axisymmetric modes. In order to gain a clearer view of the effect of heating, we have computed a third $M_j = 1.22$ case with $St = 0.6$ and $T_j/T_\infty = 2.7$. Figure 34 compares peak sound levels with peak modified instability wave energies for the three $M_j = 1.22$, $St = 0.6$ cases.

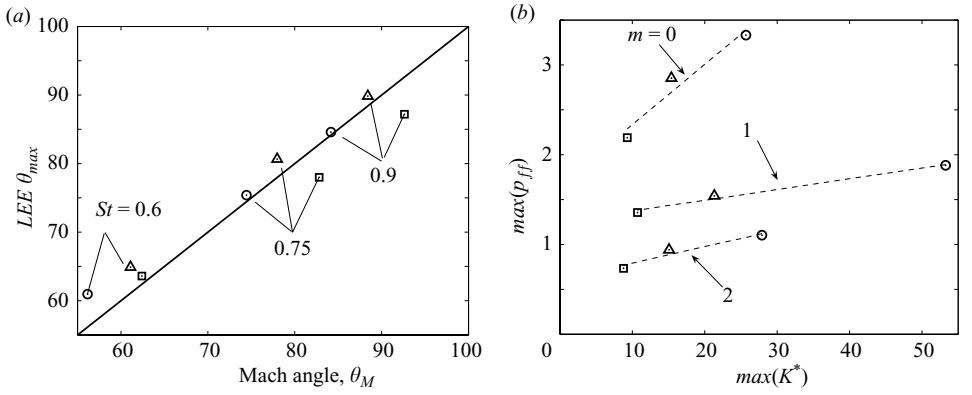

FIGURE 33. Results for hot $M_j = 1.22$ jet. (*a*) Comparison of LEE-computed peak radiation angles (θ_{max}) and Mach angles; ○, $m = 0$; △, $m = 1$, □, $m = 2$; $St = 0.6$, $St = 0.75$, $St = 0.9$ and (*b*) comparison of peak sound amplitudes and peak instability wave modified kinetic energies; ○, $St = 0.6$; △, $St = 0.75$; □, $St = 0.9$.

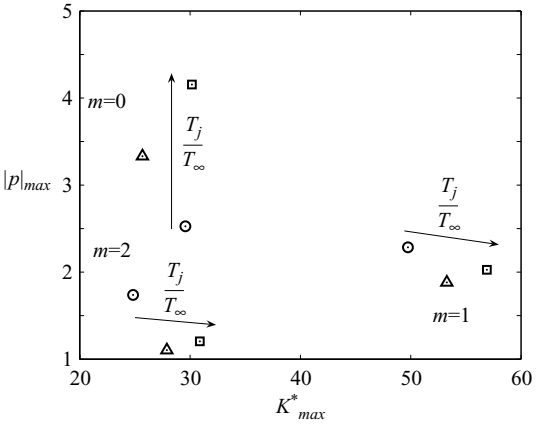

FIGURE 34. Peak sound level *vs*. peak modified instability wave energy for $M_j = 1.22$, $St = 0.6$, $T_j/T_\infty = ○, 0.77$; △, 1.7; □, 2.7.

There is a distinct amplification of the axisymmetric mode as the jet temperature is increased, while the higher modes are relatively unaffected. In general, the increased spreading rates of the hot jet mean flows result in instability waves interacting more vigorously with the (stronger) shock-cells closer to the nozzle. This leads to a general increase in source amplitudes; however, we do not see a general increase in sound amplitudes. We will use solutions to the Lilley–Goldstein equation to understand why only the axisymmetric modes show a strong increase in sound level as jet temperature is increased.

Goldstein (2001) showed that the inviscid nonlinear disturbance equations with a parallel base flow could be reduced to the third-order convective wave equation (Goldstein 1976) in terms of a nonlinear pressure variable, $\pi \equiv (p'/\overline{P})^{1/\gamma} - 1$:

$$\mathscr{L}\pi = \frac{D_0}{Dt}\frac{\partial f_j}{\partial x_j} - 2\frac{\partial \overline{U_1}}{\partial x_j}\frac{\partial f_j}{\partial x_1}, \tag{5.6a}$$

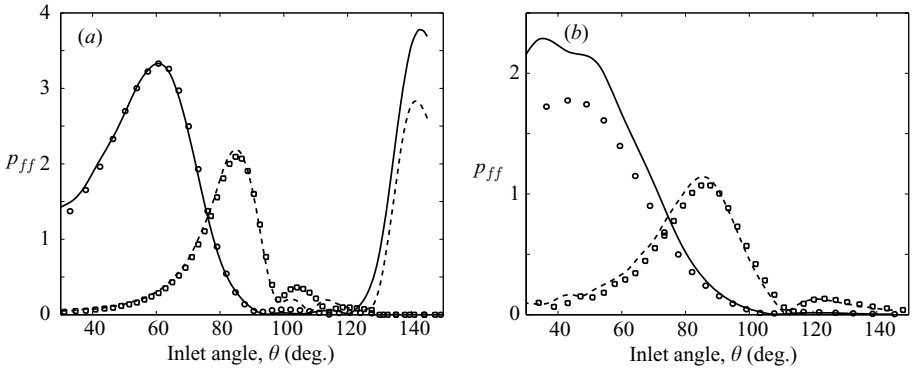

FIGURE 35. Far-field pressure, $M_j = 1.22$, (*a*) hot, $m = 0$ and (*b*) cold, $m = 1$. ——, $St = 0.6$ (LEE); - - -, $St = 0.9$ (LEE); symbols indicate LG equation solutions.

$$f_i = -\frac{\partial}{\partial x_j}(1+\pi)u_i'u_j' - (\gamma-1)T'\frac{\partial \pi}{\partial x_i}, \tag{5.6b}$$

where $\mathscr{L}$ is the third-order convective wave equation operator. We now substitute the variable decomposition (3.2) into (5.6) and expand the expression for π to obtain

$$\mathscr{L}p' = \frac{D_0}{Dt}\frac{\partial f_j}{\partial x_j} - 2\frac{\partial \overline{U_1}}{\partial x_j}\frac{\partial f_j}{\partial x_1}, \tag{5.7a}$$

$$f_i = -\frac{\partial}{\partial x_j}\left[u_i^{(t)}u_j^{(s)} + u_i^{(s)}u_j^{(t)}\right] - (\gamma-1)\left[T^{(t)}\frac{\partial p^{(s)}}{\partial x_i} + T^{(s)}\frac{\partial p^{(t)}}{\partial x_i}\right]. \tag{5.7b}$$

We have neglected a term, $\mathscr{L}(p^{(t)}p^{(s)})$. Fourier transforming these equations in x and t leads to the inhomogeneous Rayleigh equation, which we solve numerically for comparison with LEE results. This form of the equations is useful owing to the separation of f_i into what we term 'momentum' and 'thermodynamic' sources. Before using the Lilley–Goldstein (LG) equation, we should demonstrate that it is a reasonable approximation to the full problem. Figure 35 shows comparisons of the LEE and LG solutions for the $M_j = 1.22$, $m = 0$ hot and $M_j = 1.22$, $m = 1$ cold cases. While there is tangible error for the lower-frequency cold case, the LG approximation is adequate. We also note the strong downstream radiation for the LEE solution shown in figure 35(*a*). This sound is due to Mach waves associated with instability waves excited by the shock-noise sources. However, it is expected that mixing noise will be dominant at these angles.

We now examine the relative importance of the momentum and thermodynamic sources in the LG equation for the cold and heated $M_j = 1.22$ jets. Figure 36 shows LG equation solutions for $m = 0, 1$. For all cases, the momentum source is clearly the most significant. Somewhat surprisingly, heating does not seem to increase the importance of the thermodynamic terms when the temperature ratio is increased to 1.7. However, when the temperature ratio is increased to 2.7, there is a clear increase in the 'thermodynamic sound'. The most significant trend in the figure is connected to interference between the momentum and thermodynamic sound fields. For the cold axisymmetric mode, there is destructive interference between the two fields. However, as the temperature ratio is increased, the interference becomes increasingly constructive. The opposite trend is observed for $m = 1$. The cold

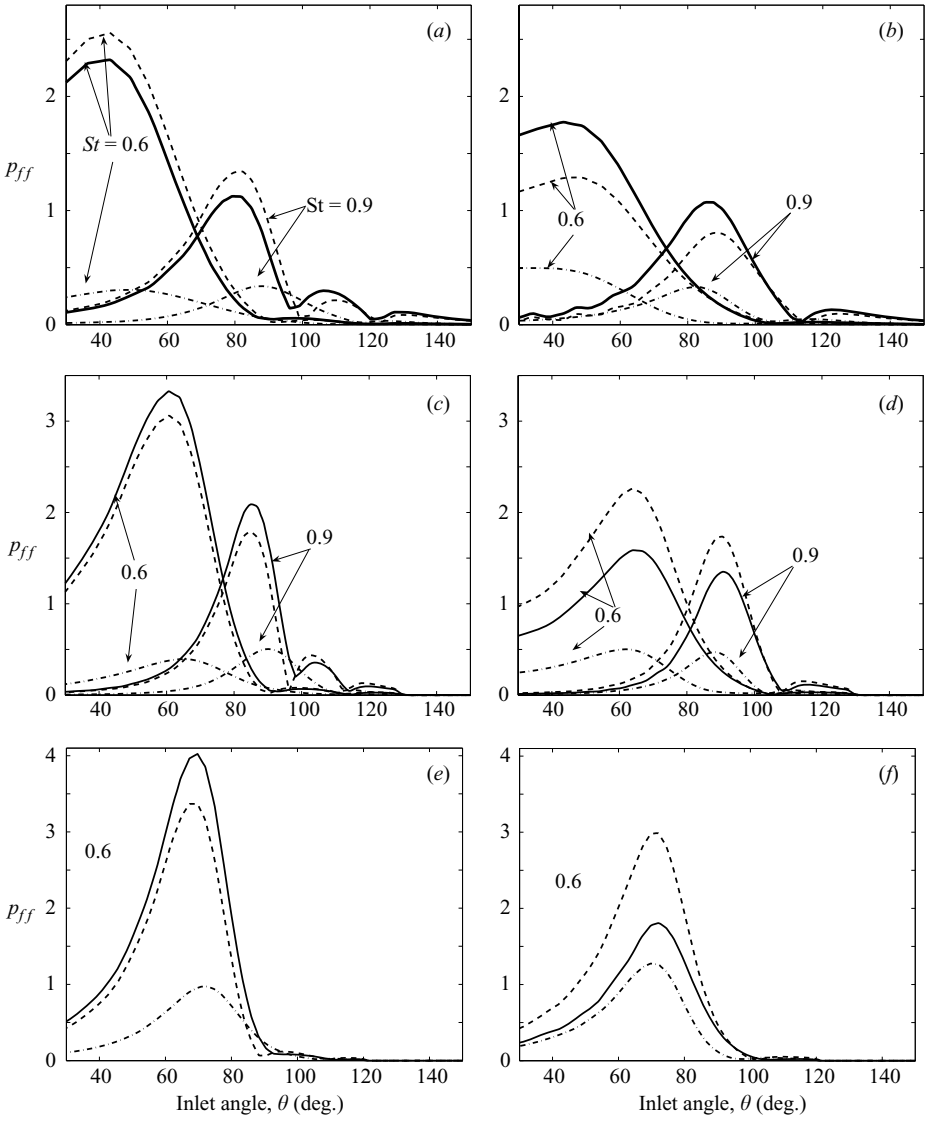

FIGURE 36. LG equation solutions for far-field pressure, $M_j = 1.22$, $St = 0.6, 0.9$, (*a*) cold, $m = 0$, *b* cold, $m = 1$, (*c*) hot, $T_j/T_\infty = 1.7$, $m = 0$, (*d*) hot, $T_j/T_\infty = 1.7$, $m = 1$, (*e*) $T_j/T_\infty = 2.7$, $m = 0$, (*f*) $T_j/T_\infty = 2.7$, $m = 1$. Sound due to: ——, full source; - - -, momentum source; —·—, thermodynamic source.

case shows constructive interference, but heating results in increasingly destructive interference. These trends provide an explanation for why the axisymmetric sound levels are elevated as the jet is heated, but the higher modes are not.

The source fields (figure 37) do not clearly indicate the degree or type of interference that will occur. However, we can see that the structure of the thermodynamic and momentum sources are similar for $m = 1$, whereas they are quite different for the axisymmetric modes. So, it is to be expected that the trends in interference will be different as observed above.

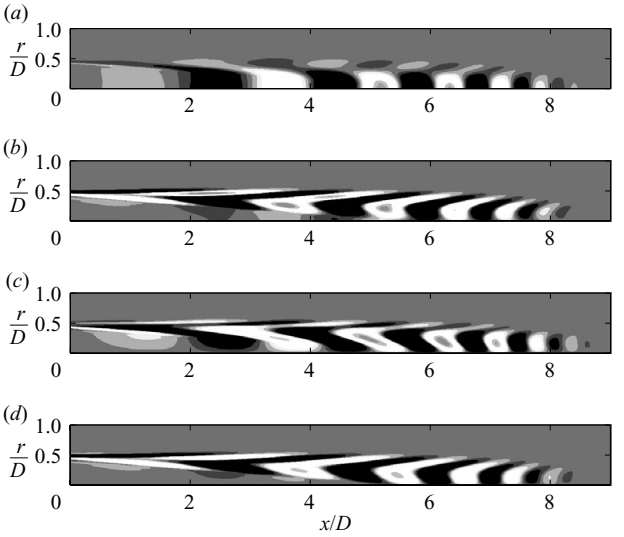

FIGURE 37. LG equation source fields for, $M_j = 1.22$, $T_j/T_\infty = 1.7$, $St = 0.6$, (*a*) momentum, $m = 0$; (*b*) thermodynamic, $m = 0$; (*c*) momentum, $m = 1$; (*d*) thermodynamic, $m = 1$. Note: different contour levels are used for each plot, the maximum levels are: (*a*) 3000, (*b*) 540, (*c*) 1000, (*d*) 660.

5.7. *Comparisons with experimental measurements*

We now move to comparisons with experiment. The far-field pressure at a given azimuthal mode number and frequency is denoted, $p_{m,\omega}$. Then, the 'total' far-field sound at a given frequency is

$$p_{ff,\omega} = \sum_{m=0}^{2} \alpha_{m,\omega} c_m |p_{m,\omega}|^2$$

where $c_0 = 1$, $c_m = 2$ for $m > 0$, and $\alpha_{m,\omega}$ is a normalization factor which specifies the spectral behaviour of instability waves at the nozzle. For simplicity, we assume a 'white noise' spectrum, i.e. each instability wave at each frequency and azimuthal mode is assumed to have the same integrated kinetic energy at the nozzle. This removes the (m, ω) dependence of $\alpha_{m,\omega}$; we set its numerical value through a simple fit to the cold $M_j = 1.22$ data – the peak value of the computed $St = 0.75$ data is set to the peak measured value. The same value for $\alpha_{m,\omega}$ is used for the cold and hot cases.

Since our computations correspond to a few discrete frequencies, conventional comparisons with experimental spectra are not possible. Instead, we take two approaches: (i) extract the relevant frequencies from the measured spectra and compare the directivity and (ii) interpolate the numerical results to intermediate frequencies and construct 'model spectra'. (These model spectra are constructed by first assuming that the dependence of the computed far-field sound on inlet angle at each frequency is a Gaussian function whose half-width is obtained from a least-squares fit. Intermediate frequency directivities are constructed as Gaussians with half-widths and amplitudes interpolated from the fits to the computed results. The model spectra are based on these model directivities.) The first approach clearly illustrates the elevation of the sound amplitudes due to shock-noise at small inlet

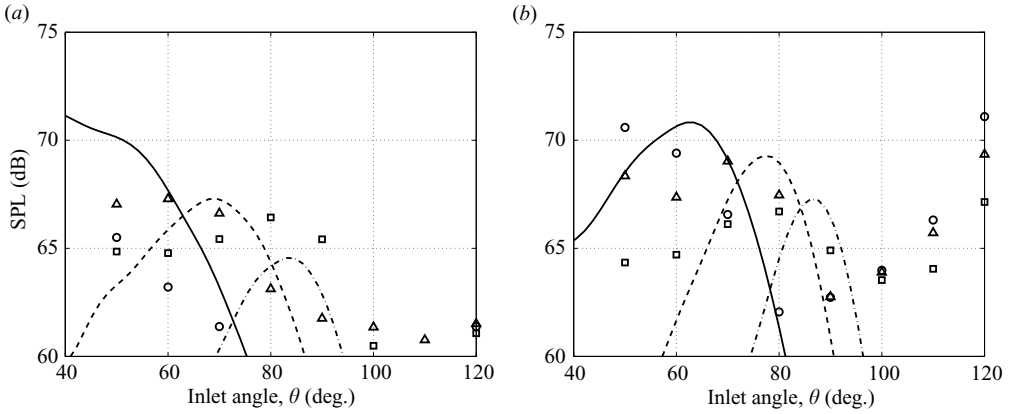

FIGURE 38. Comparison of sound pressure levels obtained from an experiment of Viswanathan (unpublished) (symbols) and computation (lines), $M_j = 1.22$, (*a*) cold and (*b*) $T_j/T_\infty = 1.7$. - - - and ○, $St = 0.6$; - - - and △, $St = 0.75$; $-\cdot-$ and □, $St = 0.9$.

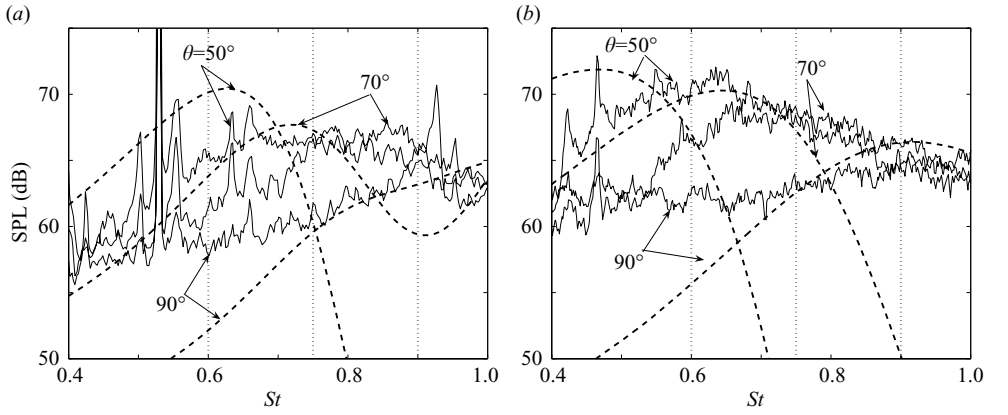

FIGURE 39. Comparison of sound pressure levels obtained from experiment of Viswanathan (——) and computation (- - -), $M_j = 1.22$, (*a*) cold and (*b*) $T_j/T_\infty = 1.7$. ——, $St = 0.6$; - - -, $St = 0.75$; $-\cdot-$, $St = 0.9$.

angles whereas the latter is the more traditional test for evaluating predictive models such as Tam (1987).

The comparisons between computation and experiment for the cold and hot $M_j = 1.22$ jets are shown in figures 38 and 39. The level of agreement is fair – the computations seem to reproduce the basic trends near the measured shock-noise peaks. However, in both cases, higher frequency sound at shallow angles is 'missing' from the computations. There are some differences in the amplitudes as well, but these are dependent on the choice of normalization. Since there are few experimental data on the distribution of energy across frequencies and azimuthal modes in turbulent jets, errors associated with the simple normalization that we have chosen should be expected. A more serious issue is the aforementioned 'missing' sound. It is possible that this discrepancy is due to 'higher-order' effects that were neglected in deriving the model problem. Specifically, nonlinear effects and the modification of instabilities by the early shock structure could alter the higher-frequency instabilities and produce stronger sound at shallower angles. Also, the peak inlet angles for the

m	x^*	$c_{ph}(x^*)/U_j$	$2\pi/k_s(x^*)$	$\theta_M(x^*)$
0	3.92, 3.60, 3.60	0.76, 0.77, 0.79	0.76, 0.78, 0.78	56.1, 74.4, 84.2
1	3.71, 3.34, 2.97	0.72, 0.74, 0.75	0.77, 0.79, 0.81	61.1, 78.0, 88.4
2	3.87, 2.66, 2.24	0.69, 0.70, 0.71	0.76, 0.82, 0.83	62.4, 82.8, 92.6

TABLE 3. Effective Mach angle parameters for the $M_j = 1.22$ hot jet. The three numbers in each table entry correspond to the frequencies $St = 0.6, 0.75, 0.9$; $c_{ph} = \omega/k_t$.

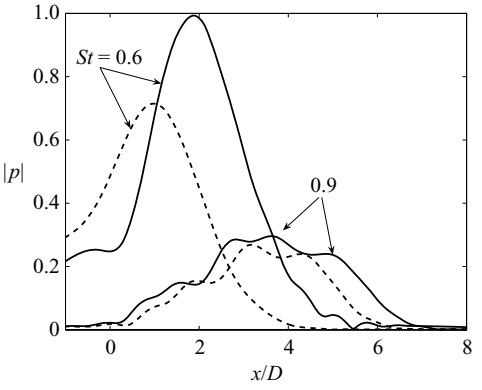

FIGURE 40. Pressure magnitude at ——, $r/D = 2.0$ and - - -, $r/D = 3.1$; $M_j = 1.22$ cold, $m = 1$.

hot case are over-predicted. Possible sources for this difference include discrepancies between computed and experimental mean flow spreading rates and the choice of turbulent Reynolds number for the PSE computations. Another possible source of error is the representation of 'moderate-frequency' turbulent disturbances as individual coherent instability waves. It is likely that less-coherent disturbances driven by some combination of nonlinear and non-modal effects will become more significant at higher frequencies. Unfortunately, since turbulent shear-layer dynamics are not well-understood, it is not possible at this time to clearly assess at what frequencies such effects become important.

It should be noted that Tam's (1987) model does not exhibit the high-frequency shallow-angle error found in our computations. The model assumes that the near-field pressure at a given frequency takes the form of a wave modulated by a Gaussian envelope. The wavelength of the pressure is based on models of the instability wave convective velocity (taken to be $0.7U_j$) and the shock-cell wavelength (an empirical formula gives $\lambda = 2\pi/k_s = 0.66$ for the cold $M_j = 1.22$ jet). Both of these values are smaller than those found from our computations (tables 2 and 3), and the the model Mach angles for $St = 0.6$ and $St = 0.9$ are $\sim 30^\circ$ and $\sim 10^\circ$ less than the computed values, respectively. There is also a significant difference in the wave envelope half-width. The model assumes that the half-width scales with frequency as $\sim 1/\omega$ whereas the computational results indicate that envelope width at $St = 0.9$ is comparable to, if not larger than, the envelope width at $St = 0.6$ (figure 40). As a result, the model directivities at higher frequencies span a broader range of angles than the computed directivities. In general, we expect the models of Harper-Bourne & Fisher (1973) and Tam (1987) to provide predictions of sound spectra which are better than

those obtained from the present approach. There are numerous parameters in our model (e.g. initial mean flow thickness, eddy viscosity) which could presumably be 'tuned' to provide better agreement with experiment. However, our primary interest has been in analysing sound generation trends and mechanisms, not the development of predictive capability, so, we have not pursued such an approach.

6. Concluding remarks

The ultimate goal of most aeroacoustics research is the reduction of undesired sound. Most attempts at jet noise control in recent years have followed a trial-and-error approach – modify the nozzle in some manner, then determine how the sound field is modified. A more direct approach is desirable, and improvements in both numerical and experimental techniques point toward the more efficient development of noise control methods. There are two distinct problems which must be solved. One of these is to understand how modification of the nozzle affects the jet turbulence. Because of limitations of computational power, for the time being this problem is best attacked experimentally. The other problem is to obtain a general physical understanding of how modifications to the turbulence influence the jet noise.

A principal goal of the present study has been to connect properties of the large-scale structures, acoustic sources and sound fields – thus attacking the second problem mentioned above. An array of computational tools has been developed to generate and analyse the various components of the instability wave/shock-cell interaction problem. We examined shock-noise source spectra and applied a filter to isolate the radiating components. Unfiltered sources containing several shock modes showed spatial localization lending support to the point-source modelling assumption of Harper-Bourne & Fisher (1973). Filtered sources were spatially distributed in agreement with the experimental study of Norum & Seiner (1982*a*). It was shown that solutions to an inhomogeneous Rayleigh equation (obtained by neglecting the effect of mean flow spreading on sound propagation) provided excellent approximations to the 'full' problem. We then examined the importance of individual source terms in the Rayleigh equation. We found that the mass source was dominant for the axisymmetric and $m = 2$ modes whereas the radial-momentum source was dominant for the $m = 1$ mode. We also found that interference between the different sources was significant for $m = 2$. These results suggest that there are significant differences in the physical sound-generation mechanisms for the azimuthal modes. The Tam & Tanna (1982) Mach angle model was used to identify a range of angles at which Mach waves could 'potentially' radiate. The shock-noise sources were then used to define an effective Mach angle which provided a prediction of the peak radiation angle. For almost all of the cases considered, the predictions showed good agreement with the computed results. We also showed that there was a consistent correlation between peak instability wave and shock-noise amplitudes (for most cases) and concluded that the radial structure of the axisymmetric modes (specifically its penetration into the jet core) leads to 'more efficient' sound generation than the higher modes. This increased efficiency was amplified when the jet temperature was increased. Solutions to a Lilley–Goldstein equation showed that sound from thermodynamic sources increased in significance as the jet was heated, and constructive interference between the thermodynamic sources and momentum sources led to a substantial increase in sound levels for the axisymmetric modes. However, higher modes showed destructive interference between sound radiated by momentum and thermodynamic sources which resulted in sound fields which were little-affected by heating.

In our approach to this problem, we have applied numerical tools of low or moderate expense to a model problem formulated by Tam (1987). An important advantage of this formulation is that it results in an unambiguous definition of the sound sources which, in turn, allows for a more detailed examination of sound generation than currently allowed by costlier approaches such as LES and DNS. In these 'direct' approaches, there is a real difficulty in extracting the physical sound-generation mechanisms from complex three-dimensional flow fields. It is hoped that the current study and future direct, less-approximate, numerical solutions will complement each other. The results obtained here can provide an analytical framework for understanding the simulation results, and full, accurate simulations can provide insight into the validity of the modelling assumptions used in this study.

Finally, we mention two outstanding issues whose study would (hopefully) lead to a better understanding of shock-noise. First, comparisons with experiments show that higher-frequency sound at shallow angles is 'missing' from our computations. Is this due to the linear instability wave representation of turbulence, or are other modelling assumptions responsible? Experimental measurements (of velocity, ideally) decomposed into azimuthal modes and frequencies (as in Suzuki & Colonius 2006) would provide means for assessing models such as the instability waves used here while also giving a clearer picture of turbulent shear-layer dynamics. The second issue centres on the difference between 'real' commercial engine exhausts and the single-stream jets considered here. Reduction of shock-noise requires the consideration of coannular jets with flight streams (such as those studied experimentally by Viswanathan 2004). The application of the methods used in this work to realistic multiple-stream jets presents a number of significant computational and analytical challenges. The present study provides a necessary first step towards analysis of these realistic configurations.

We would like to thank Dr K. Viswanathan for providing experimental results and Dr L. Cheung for providing his PSE code and generously lending assistance with the PSE calculations. This study was supported by Boeing. P. K. R. also received support from an NDSEG fellowship.

Appendix A. Numerical method for linearized Euler equations

Here, we present a few of the numerical details omitted from § 3.5.

A.1. *Spectral filter*

The exponential filter function (Majda *et al.* 1978; Gottlieb & Hesthaven 2001) is:

$$\sigma_j = \exp\left[-\ln(\epsilon_M)\left(\frac{j}{N}\right)^{2p}\right], \tag{A 1}$$

where ϵ_M is machine zero (usually taken as 1.0×10^{16}), N is the number of grid points, $j = 1, \ldots, N$, and $2p$ is the filter order. We used $p = 15$ for all shock-noise computations (both directions and subdomains) except for cases with azimuthal mode number $m = 2$ for which $p = 10$ was used.

A.2. *Damping layers*

The damping layers applied at the inflow, outflow and top of the computational domain use cubic damping functions (Manning 1999). For example, at the outflow,

the governing equations are modified to be:

$$\frac{\partial Q_i}{\partial t} = RHS_i + \mathrm{d}(x)Q_i, \tag{A 2}$$

with damping function $\mathrm{d}(x)$ defined as:

$$\mathrm{d}(x) = \begin{cases} d_0\left(\dfrac{x - x_0}{x_f - x_0}\right)^3, & x > x_0, \\ 0, & x < x_0, \end{cases} \tag{A 3}$$

where d_0 is the 'strength' of the damping, x_0 is the starting point of the layer, and x_f is the outflow boundary. The sizes of the damping layers used in the $M_j = 1.22$ shock-noise computations presented earlier are shown in figure 3. At higher Mach number ($M_j = 1.36$) the outflow sponge began at $x = 11$ rather than $x = 9$. At the inflow and top layers, the sponge strength for all cases was $d_0 = 4$; at the outflow we used $d_0 = 6$.

A.3. *Grid mappings*

As mentioned earlier, the computational grids are the Gauss–Lobatto points,

$$z_j = \cos\left(\frac{j\pi}{N}\right) \qquad (0 \leqslant j \leqslant N). \tag{A 4}$$

The Bayliss & Turkel (1992) mapping used for the radial direction in the inner subdomain is:

$$r = \left(1 - \alpha_2 - \frac{1}{\alpha_1}\tan[\lambda(z - z_0)]\right)L/2, \tag{A 5}$$

$$\lambda = \frac{\tan^{-1}[\alpha_1(1 - \alpha_2)]}{1 - z_0}, \tag{A 6}$$

$$z_0 = \frac{\kappa - 1}{\kappa + 1}, \tag{A 7}$$

$$\kappa = \frac{\tan^{-1}[\alpha_1(1 + \alpha_2)]}{\tan^{-1}[\alpha_1(1 - \alpha_2)]}, \tag{A 8}$$

where L is the size of the physical domain. This mapping clusters grid points in the shear layer about $r^* = (1 - \alpha_2)L/2$, and α_1 sets the amount of clustering. The Kosloff & Tal-ezer (1993) mapping used for the outer subdomain radial mapping and streamwise mapping is:

$$x = \left(1 + \frac{\sin^{-1}(\beta z)}{\sin^{-1}(\beta)}\right)L/2. \tag{A 9}$$

This mapping reduces the Gauss–Lobatto boundary clustering; as β increases, the grid distribution becomes more uniform, but the Chebyshev approximation error increases as well. Hesthaven, Dinesen & Lynov (1999) recommend setting $\beta = \cos(0.5)$ to balance these competing effects, and we follow their recommendation here. Unless noted otherwise, all shock-noise computations in this work used: 181 grid points in the inner subdomain with $\alpha_1 = 4.0$, $\alpha_2 = 0.5$; 65 grid points in the outer subdomain; and 513 grid points in the streamwise direction. The domain sizes are shown in figure 3.

Near-boundary clustering in the streamwise direction is a tangible deficiency of the present method. Though we have not pursued it here, adding subdomains in the

streamwise direction would potentially allow for significant increases in computational efficiency and flexibility.

Finally, we note that the time-step was $\Delta t = 0.0004$ for cases with $m = 0, 1$ and $\Delta t = 0.0003$ for $m = 2$.

Appendix B. The compressible Rayleigh equation

This Appendix presents the compressible Rayleigh equation and describes how numerical solutions were obtained. We focus on the computation of the far-field sound. Rayleigh equation solutions were used in this study for several tasks including: validation of the LEE code; assessing the effect of mean flow spreading on shock-noise radiation; and assessing the significance of individual shock-noise source terms.

B.1. *Formulation*

We begin with the inhomogeneous linearized Euler equations in cylindrical coordinates and assume a parallel base flow, $\overline{U}_x(r)$. Taking a Fourier series expansion in the azimuthal direction, and applying Fourier transforms in time and the streamwise direction,

$$p = \sum_{m=-\infty}^{\infty} \hat{p}_m \, \mathrm{e}^{\mathrm{i}m\phi}, \tag{B 1a}$$

$$\tilde{p}(k, r, \omega, m) = \int_{-\infty}^{\infty} \int_{-\infty}^{\infty} \hat{p}_m(x, r, t) \, \mathrm{e}^{-\mathrm{i}(kx+\omega t)} \, \mathrm{d}x \, \mathrm{d}t, \tag{B 1b}$$

we can combine the resulting equations into the inhomogeneous compressible Rayleigh equation:

$$\frac{\overline{n}^2}{r} \frac{\mathrm{d}}{\mathrm{d}r} \left(\frac{r}{\overline{n}^2} \overline{a}^2 \frac{\mathrm{d}\tilde{p}}{\mathrm{d}r} \right) + \omega^2 \left[\overline{n}^2 - \overline{a}^2 \left(\kappa^2 + \frac{m^2}{r^2 \omega^2} \right) \right] \tilde{p} = \tilde{S}(k, r, m, \omega), \tag{B 2}$$

where $\kappa \equiv k/\omega$, $\overline{n} \equiv 1 + \overline{U}_x \kappa$, and $\overline{a}$ is the mean speed of sound. First, consider the solution outside of the shear layer. If $\overline{U}_x \to 0$, $\overline{a} \to 1$, and $\tilde{S} \to 0$, (B 2) reduces to Bessel's equation. Applying a radiation condition then gives the following far-field solution:

$$\tilde{p}_{outer} = C(\kappa) H_m^{(2)}(\sqrt{1 - \kappa^2} \omega r), \tag{B 3}$$

where C is a factor that depends on the inner solution and $H_m^{(2)}$ is the Hankel function of the second kind. In order to return to physical space, an inverse Fourier transform in k must be applied to $\tilde{p}$. As $z \to \infty$, $H_m^{(2)}(z) \sim \sqrt{(2/\pi z)} \exp(-\mathrm{i}(z - (1/2) m\pi - \pi/4))$. Now if we introduce spherical coordinates (R, ψ, ϕ) and allow $\omega R \to \infty$, the inverse Fourier integral can be evaluated by the method of stationary phase with the final result (in the frequency domain):

$$\kappa = -\cos(\psi), \tag{B 4a}$$

$$p_{ff,\omega} \sim \frac{\mathrm{i}C(\kappa = -\cos(\psi))}{\pi R} \, \mathrm{e}^{-\mathrm{i}\omega R}. \tag{B 4b}$$

Rather than solving (B 2) with finite source terms, we first solve for the Green's function, $\tilde{G}(r; r_0)$, defined by

$$\frac{\overline{n}^2}{r} \frac{\mathrm{d}}{\mathrm{d}r} \left(\frac{r}{\overline{n}^2} \overline{a}^2 \frac{\mathrm{d}\tilde{G}(r; r_0)}{\mathrm{d}r} \right) + \omega^2 \left[\overline{n}^2 - \overline{a}^2 \left(\kappa^2 + \frac{m^2}{r^2 \omega^2} \right) \right] \tilde{G}(r; r_0) = \frac{\delta(r - r_0)}{r}. \tag{B 5}$$

Having solved for $\tilde{G}$, the pressure is found from a simple convolution integral:

$$\tilde{p}(r) = \int_0^\infty \tilde{G}(r\,;r_0)\tilde{S}(r_0)r_0\,\mathrm{d}r_0. \tag{B 6}$$

This solution outside of the shear layer can be used with (B 3) to obtain $C(\kappa)$. Then, the far-field sound is found from (B 4).

B.2. *Numerical method*

In the context of linear stability theory, the Rayleigh equation is set up as an eigenvalue problem which is solved by the shooting method. In our case, what would be the eigenvalue, κ, is known to vary continuously between -1 and 1 as $\cos(\psi)$. With this understood, we can still adopt the shooting method while dropping the eigenvalue aspect and adding modifications to account for the singular nature of (B 5).

The inner and outer solutions with which to start the shooting method are the Bessel function of the first kind and the Hankel function of the second kind. The outer and inner solution are computed up to the source location, r_0. At the source locations, jump conditions based on (B 5) are applied:

$$\tilde{G}^+ - \tilde{G}^- = 0, \tag{B 7a}$$

$$\frac{\mathrm{d}\tilde{G}^+}{\mathrm{d}r} - \frac{\mathrm{d}\tilde{G}^-}{\mathrm{d}r} = r_0\overline{a}^2(r_0). \tag{B 7b}$$

After the outer solution is scaled based on (B 7), the method of stationary phase can be applied as outlined in the previous section to obtain the far-field Green's function. Typically, the computation of (B 6) requires the solution of (B 5) for several values of r_0. However, if we use the reciprocity relation,

$$\frac{\tilde{G}(r_0\,;r_s)}{\overline{n}(r_0)^2} = \frac{\tilde{G}(r_s\,;r_0)}{\overline{n}(r_s)^2}, \tag{B 8}$$

and take r_s as a point outside the shear layer where mean flow gradients are small, we need only one Rayleigh equation solution to obtain the far-field sound at a given angle. Specifically, taking r_s to be well outside the shear layer, computing $\tilde{G}(r, r_s)$ gives $\tilde{G}(r_s, r)$ which can be inserted into (B 6) to obtain $\tilde{p}(r_s)$ which can then be extended to the far field. This Green's function solution is similar to the 'separation of variables' solution for the far-field Green's function given by Tam & Auriault (1998). Near-field solutions for the Green's function are discussed by Agarwal, Morris & Mani (2004) within the broader context of instability-wave suppression in linear aeroacoustic computations.

REFERENCES

Agarwal, A., Morris, P. J. & Mani, R. 2004 Calculation of sound propagation in nonuniform flows: suppression of instability waves. *AIAA J.* **42**, 80–88.

Balakumar, P. 1998 Prediction of supersonic jet noise. *AIAA Paper* 1998-1057.

Bayliss, A. & Turkel, E. 1992 Mappings and accuracy for Chebyshev pseudo-spectral approximations. *J. Comput. Phys.* **101**, 349–359.

Cheung, L. C. & Lele, S. K. 2004 Acoustic radiation from subsonic and supersonic mixing layers with nonlinear PSE. *AIAA Paper* 2004-0363.

Colonius, T. & Lele, S. K. 2004 Computational aeroacoustics: progress on nolinear problems of sound generation. *Prog. Aerospace Sci.* **40**, 345–416.

Conte, S. D. 1966 The numerical solution of linear boundary value problems. *SIAM Rev.* **8**, 309–321.

Freund, J. B. 2001 Noise sources in a low-Reynolds-number turbulent jet at Mach 0.9. *J. Fluid Mech.* **438**, 277–305.

Goldstein, M. E. 1976 *Aeroacoustics*. McGraw–Hill.

Goldstein, M. E. 2001 An exact form of Lilley's equation with a velocity quadrupole/temperature dipole source term. *J. Fluid Mech.* **443**, 231–236.

Gottlieb, D. & Hesthaven, J. S. 2001 Spectral methods for hyperbolic problems. *J. Comput. Appl. Maths* **128**, 83–131.

Hanifi, A., Schmid, P. J. & Henningson, D. S. 1996 Transient growth in compressible boundary layer flow. *Phys. Fluids* **8**, 51–65.

Harper-Bourne, M. & Fisher, M. J. 1973 The noise from shock waves in supersonic jets. In *AGARD Conf. Proc.* **131**, 11.1–11.13.

Herbert, T. 1997 Parabolized stability equations. *Annu. Rev. Fluid Mech.* **29**, 245–283.

Hesthaven, J. S. 1997 A stable penalty method for the compressible Navier–Stokes equations: II. One-dimensional domain decomposition schemes. *SIAM J. Sci. Comput.* **18**, 658–685.

Hesthaven, J. S., Dinesen, P. G. & Lynov, J. P. 1999 Spectral collocation time-domain modeling of diffractive optical elements. *J. Comput. Phys.* **155**, 287–306.

Howe, M. S. & Ffowcs Williams, J. E. 1978 On the noise generated by an imperfectly expanded supersonic jet. *Phil. Trans. R. Soc. Lond.* A **289**, 271–314.

Hu, F. Q., Hussaini, M. Y. & Manthey, J. 1996 Low-dissipation and low-dispersion Runge–Kutta schemes for computational acoustics. *J. Comput. Phys.* **124**, 177–191.

Kosloff, D. & Tal-ezer, H. 1993 A modified Chebyshev pseudospectral method with an $O(N\text{-}1)$ time step restriction. *J. Comput. Phys.* **104**, 457–469.

Li, F. & Malik, M. R. 1994 Mathematical nature of parabolized stability equations. In *Laminar–Turbulent Transition*, pp. 205–212. Springer.

Lighthill, M. J. 1952 On sound generated aerodynamically I. General theory. *Proc. R. Soc. Lond.* A **222**, 1–32.

Lui, C. C. M. 2003 A numerical investigation of shock-associated noise. PhD dissertation, Stanford University.

Majda, A., McDonough, J. & Osher, S. 1978 The Fourier method for nonsmooth initial data. *Maths Comput.* **32**, 1041–1081.

Malik, M. R. & Chang, C. L. 2000 Nonparallel and nonlinear stability of supersonic jet flow. *Computers Fluids* **29**, 327–365.

Manning, T. A. 1999 A numerical investigation of sound generation in supersonic jet screech. PhD dissertation, Department of Aeronautics and Astronautics, Stanford University.

Norum, T. D. & Seiner, J. M. 1982*a* Broadband shock noise from supersonic jets. *AIAA J.* **20**, 68–73.

Norum, T. D. & Seiner, J. M. 1982*b* Measurements of mean static pressure and far field acoustics of shock-containing supersonic jets. *NASA TM* 84521.

Powell, A. 1953 On the mechanism of choked jet noise. *Proc. Phys. Soc. Lond.* **66**, 1039–1056.

Raman, G. 1999 Supersonic jet screech: half century from Powell to the present. *J. Sound Vib.* **225**, 543–571.

Ray, P. K. 2006 Sound generated by instability wave/shock-cell interaction in supersonic jets. PhD dissertation, Department of Mechanical Engineering, Stanford University. (Electronic copies of this report may be obtained from the authors.)

Stanescu, D. & Habashi, W. G. 1998 $2N$-storage low dissipation and dispersion Runge–Kutta schemes for computational acoustics. *J. Comput. Phys.* **143**, 674–681.

Suzuki, T. & Colonius, T. 2006 Instability waves in a subsonic round jet detected using a near-field phased microphone array. *J. Fluid Mech.* **565**, 197–226.

Tam, C. K. W. 1987 Stochastic model theory of broadband shock associated noise from supersonic jets. *J. Sound Vib.* **116**, 265–302.

Tam, C. K. W. 1990 Broadband shock-associated noise of moderately imperfectly expanded supersonic jets. *J. Sound Vib.* **140**, 55–71.

Tam, C. K. W. 1991 Broadband shock-associated noise from supersonic jets in flight. *J. Sound Vib.* **151**, 131–147.

Tam, C. K. W. 1995 Supersonic jet noise. *Annu. Rev. Fluid Mech.* **27**, 17–43.

Tam, C. K. W. & Auriault, L. 1998 Mean flow refraction effects on sound radiated from localized sources in a jet. *J. Fluid Mech.* **370**, 149–174.

Tam, C. K. W. & Tanna, H. K. 1982 Shock associated noise of supersonic jets from convergent–divergent nozzles. *J. Sound Vib.* **81**, 337–358.

Tam, C. K. W., Jackson, J. A. & Seiner, J. M. 1985 A multiple-scales model of the shock-cell structure of imperfectly expanded supersonic jets. *J. Fluid Mech.* **153**, 123–149.

Tanna, H. K. 1977 An experimental study of jet noise. Part II: Shock associated noise. *J. Sound Vib.* **50**, 426–444.

Thies, A. T. & Tam, C. K. W. 1996 Computation of turbulent axisymmetric and nonaxisymmetric jet flows using the $k-\epsilon$ model. *AIAA J.* **34**, 309–316.

Viswanathan, K. 2004 Parametric study of noise from dual-stream nozzles. *J. Fluid Mech.* **521**, 35–68.

Wilcox, D. C. 1993 *Turbulence Modeling for CFD*. DCW Industries.

Wishart, D. P. 1995 The structure of a heated supersonic jet operating at design and off-design conditions. PhD dissertation, Florida State University.

Yen, C.-C. & Messersmith, N. L. 1999 The use of compressible parabolized stability equations for prediction of jet instabilities and noise. *AIAA Paper* 1999-1859.